The heat transfer potential of compressor vanes on a hydrogen fueled turbofan engine

Applied Thermal Engineering 236 (2024) 121722

Contents lists available at ScienceDirect

Applied Thermal Engineering

journal homepage: www.elsevier.com/locate/apthermeng

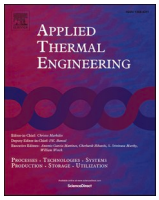

Research Paper

The heat transfer potential of compressor vanes on a hydrogen fueled turbofan engine

Alexandre Capitao Patrao [a,*], Isak Jonsson [a], Carlos Xisto [a], Anders Lundbladh [a,b], Marcus Lejon [b], Tomas Grönstedt [a]

[a] Chalmers University of Technology, Gothenburg SE-41296, Sweden
[b] GKN Aerospace Sweden, Trollhättan SE-46181, Sweden

ARTICLE INFO

Keywords:
Hydrogen
Heat transfer
Cryogenics
Compressor
CFD
Emissions

ABSTRACT

Hydrogen is a promising fuel for future aviation due to its CO_2-free combustion. In addition, its excellent cooling properties as it is heated from cryogenic conditions to the appropriate combustion temperatures provides a multitude of opportunities. This paper investigates the heat transfer potential of stator surfaces in a modern high-speed low-pressure compressor by incorporating cooling channels within the stator vane surfaces, where hydrogen is allowed to flow and cool the engine core air. Computational Fluid Dynamics simulations were carried out to assess the aerothermal performance of this cooled compressor and were compared to heat transfer correlations. A core air temperature drop of 9.5 K was observed for this cooling channel design while being relatively insensitive to the thermal conductivity of the vane and cooling channel wall thickness. The thermal resistance was dominated by the air-side convective heat transfer, and more surface area on the air-side would therefore be required in order to increase overall heat flow. While good agreement with established heat transfer correlations was found for both turbulent and transitional flow, the correlation for the transitional case yielded decent accuracy only as long as the flow remains attached, and while transition was dominated by the bypass mode. A system level analysis, indicated a limited but favorable impact at engine performance level, amounting to a specific fuel consumption improvement of up to 0.8 % in cruise and an estimated reduction of 3.6 % in cruise NOx. The results clearly show that, although it is possible to achieve high heat transfer rate per unit area in compressor vanes, the impact on cycle performance is constrained by the limited available wetted area in the low-pressure compressor.

1. Introduction

Hydrogen is being considered as a candidate for new sustainable fuels in order meet the ambitious environmental target set forth by the European Union (EU) in the European Green Deal, namely ensuring an economy with no net greenhouse emissions by 2050 [1]. The advantages of hydrogen include CO2-free combustion and higher gravimetric energy density compared to kerosene. The challenges of using hydrogen in conventional transport aircraft relate mainly to its cryogenic storage temperature and lower density, which impact the size, mass, and amount of insulation of the propellant feed system [2]. However, the cryogenic temperatures coupled with the high specific heat capacity of hydrogen result in an exceptional coolant with the potential to be used as a heat sink for the engine [3–5].

The amount of heat which cryogenic hydrogen can absorb is considerable and could lead to substantial reductions in specific fuel consumption (SFC). For instance, when increasing the hydrogen temperature from 25 K to a compressor outlet temperature of 800 K, the energy content per kilogram of fuel amounts to about 10 % of the fuel heating value. Theoretically, in a loss-free system, this alone has the potential to reduce the engine SFC by 10 % [6].

Hydrogen can be used in a compressor through pre-cooling, intercooling, or continuous cooling along the flow path. Pre-cooling can be achieved by placing a heat exchanger before the low pressure compressor (LPC) inlet or by using its inlet guide vane [3–5,7,8]. Intercooling can be carried out by similar means between the LPC and high-pressure compressor (HPC) if heat exchangers are placed in the intermediate compressor duct (ICD) [6,9,10]. Continuous cooling where each stator in the LPC is used for heat transfer provides the largest performance improvement but features a high degree of complexity [11–13]. Cooling the compressor core air will also increase the fuel

* Corresponding author.
E-mail addresses: capitao@chalmers.se, alexandre.capitaopatrao@gknaerospace.com (A. Capitao Patrao).

https://doi.org/10.1016/j.applthermaleng.2023.121722
Received 23 May 2023; Received in revised form 13 September 2023; Accepted 30 September 2023
Available online 2 October 2023

Nomenclature

AR	Aspect Ratio
BPR	Bypass Ratio
c	Airfoil chord [m]
C_p	Pressure coefficient
CEA	Chemical Equilibrium Applications
CFD	Computational Fluid Dynamics
C_{max}	Maximum heat capacity of the fluids in a HEX [J/K]
C_{min}	Minimum heat capacity of the fluids in a HEX [J/K]
C_r	Ratio of heat capacities C_{min}/C_{max}
DR	Degree of Reaction
EINOx	Emission index of NOx [g/kg]
ϵ	Heat exchanger effectiveness
η_p	Polytropic Efficiency
f	Friction factor
FPR	Fan Pressure Ratio
γ	Intermittency
GESTPAN	GEneral Stationary and Transient Propulsion ANalysis
h	Convective heat transfer coefficient $[W/m^2K]$
HEX	Heat exchanger
HPC	High Pressure Compressor
HPT	High Pressure Turbine
HTR	Hub to Tip Ratio
ICD	Intermediate Compressor Duct
IGV	Inlet Guide Vane
ISA	International Standard Atmosphere
k	Thermal conductivity of vane [W/mK]
$\widetilde{k}$	Turbulent kinetic energy [J/kg]
λ	HPC or HPT last blade height [m]
LPC	Low Pressure Compressor
MCL	Maximum climb
MHP	Multi-hole Probe
MTO	Maximum take-off
NIST	National Institute of Standards and Technology
NOx	Nitrogen oxides
NTU	Heat exchanger number of transfer units
Nu	Nusselt number
OGV	Outlet Guide Vane
OPR	Overall Pressure Ratio
$\widetilde{\omega}$	Turbulence frequency [1/s]
p	Pressure [bar]
ϕ	Equivalence ratio
Π	Correction factor for polytropic efficiency
Pr	Prandtl number
PR	Pressure Ratio
PS	Pressure side
ψ	Stage loading
Q	Heat flow [W]
R	Thermal resistance $[m^2K/W]$
Re	Reynolds Number
$\widetilde{Re}_{\theta t}$	Transition momentum thickness Reynolds number
SFC	Specific Fuel Consumption [mg/Ns]
σ	Calibration factor for critical Reynolds number
SS	Suction side
T	Temperature [K]
t	Cooling channel wall thickness [m]
TOC	Top of climb
Tu	Turbulence intensity
U	Heat transfer coefficient $[W/m^2K]$
x	Surface coordinate in streamwise direction [m]
ξ	Total pressure loss coefficient
y^+	Dimensionless wall distance

Subscripts

Crit	At transition conditions
Dyn	Dynamic component
∞	Freestream conditions
lam	Laminar
mid	Mid-point conditions in the cooling process
P	Polytropic
trans	Transition
turb	Turbulent
wall	Wall conditions
x	Evaluated at a distance x from the leading edge
0	Stagnation conditions

enthalpy prior to combustion and increases the core specific work [14] (for constant thrust and HPC discharge temperature). Shah and Tan [15] showed that it is possible for a cooled compressor to increase its pressure ratio, maximum mass flow capability, and efficiency and Liu et al. [16] showed that cooling decreases laminar separation and delays turbulent separation.

Compressor heat transfer studies were carried out by Dijk et al. [12] which investigated various methods for stator cooling, including cooling of the vane base and channel cooling. The main benefit of employing existing stator surfaces for cooling is to avoid adding additional wetted surface in the engine flow path or rerouting core air to additional heat exchangers. The study concluded that the small surface areas on the hydrogen side limited the amount of obtainable heat transfer. Although the study by Dijk et al. [12] provided a good insight into the potential of using compressor surfaces for heat-transfer, it did not account for the effect of laminar-turbulent transition on the boundary layer thermal resistance. Ito and Nagasaki [17] suggested using supercritical carbon dioxide as the coolant in an intercooled-recuperated engine, where the absorbed heat from intercooling is ejected into the bypass stream and recuperated heat from the turbine exhaust is transferred into the core air stream at the last stages of the HPC. System level calculations showed a maximum decrease in SFC of approximately 6 % and thrust increase of 11 %.

This paper complements existing work by evaluating the cooling potential for hydrogen using a bottom-up approach, starting from a detailed flow and thermal analysis at component level of a modern LPC with stator cooling. Insights from this level of analysis will then inform system level calculations and impact engine cycle performance.

First, a comparison is carried out between numerical and experimental results in order to verify the applicability of the employed CFD setup. This is performed using experimental data from the low-pressure compressor test facility, a rig built at Chalmers University of Technology with the aim to validate heat management concepts for multistage compression systems [18–20]. The experimental test rig has similar design parameters as the final two stages of a modern, multi-stage, high-speed LPC [21].

The compressor is then investigated numerically at more representative engine conditions to assess its heat transfer potential, since it is more typical of a modern, high-speed, high-efficiency design. Cooling is incorporated into this compressor design by including cooling channels underneath the stator vane surfaces, hence providing a heat sink to the core air stream without incurring any additional pressure losses. CFD and heat transfer analyses are performed which consider the impact of laminar-turbulent transition on heat transfer. Correlations will be tuned to these CFD simulations and used in system level calculations. The paper is concluded with an investigation of the impact of the intercooled

integrated compressor unit on engine performance.

The present study builds on previous attempts to establish the heat transfer potential of compressor vanes for the purpose of intercooling. It expands on that work through the inclusion of a more detailed numerical study on the aerothermal performance of compressor vanes, including important phenomena such as transition and the impact of cooling in the multi-stage performance of the compressor. The study relies on validated CFD models to predict the aerodynamic performance, increasing the confidence on the results. These findings are incorporated into a system level model to assess the impact in terms of SFC and NOx-emissions on a future hydrogen-fueled turbofan engine.

2. Methodology

This section starts with introducing the LPC geometry used for assessing the heat transfer potential of existing aero surfaces by means of CFD simulations and aerothermal analyses. The next subsection concerns the CFD modeling used, followed by a section describing the low-speed compressor test facility at Chalmers which provides experimental data for CFD validation. This section concludes with a review of the engine system model used for evaluating the impact of intercooling on engine performance.

2.1. Geometry

The compressor design [21], referred to as the VINK compressor, is used for evaluating the heat transfer potential of hydrogen cooling in an LPC. It is a 3 stage, lightly loaded, high-speed, low-pressure compressor with a design pressure ratio of 2.8 and is part of a year 2035 large, geared turbofan engine, providing a thrust of 70,000 lbf at sea level static conditions. The geometry of this LPC is shown in Fig. 1 and is open access and available for download [22]. The design effort for this engine was a collaboration between Swedish academic institutions and industry which aimed at demonstrating the national capability of developing a modern compressor design from scratch.

2.2. CFD modeling

The numerical models and methods employed in the aerothermal analyses of the VINK geometry will be described in this section of the paper. ANSYS Turbogrid has been used to generate structured, hexahedral meshes, an image of which is shown in Fig. 2. The mesh is sufficiently refined near the walls to adhere to $y^+ < 1$ for the first wall node and results for the conducted mesh studies will be presented in section 3.2.1.

The flow field was simulated using the solver ANSYS CFX 2021r1, which solves the compressible Reynolds Averaged Navier-Stokes (RANS) equations together with the k − ω SST turbulence model. The effect of transition on heat transfer was investigated in one specific case, and used the two-equation Gamma-Theta transition model, which has been developed to cover a wide range of transitional flows, including bypass transition [23–25]. The governing equations are summarized in Eq. (11), and additional terms and model constants are given in [26]. The working fluid was set as a calorically perfect gas with temperature dependent thermal conductivity and viscosity, implemented using polynomials fitted to data from NIST REFPROP [27].

$$\frac{\partial \boldsymbol{Q}}{\partial t}+\frac{\partial \boldsymbol{F}_j}{\partial x_j}=\boldsymbol{H} \tag{1}$$

$$\boldsymbol{Q}=\begin{bmatrix}\overline{\rho}\\ \overline{\rho}\widetilde{u}_i\\ \overline{\rho}\widetilde{h}_0-\overline{p}\\ \overline{\rho}\widetilde{k}\\ \overline{\rho}\widetilde{\omega}\\ \overline{\rho}\gamma\\ \overline{\rho}\widetilde{Re}_{\theta t}\end{bmatrix}\quad \boldsymbol{F}_j=\begin{bmatrix}\overline{\rho}\widetilde{u}_j\\ \overline{\rho}\widetilde{u}_j\widetilde{u}_i+\overline{p}\delta_{ij}-\tau_{ij}\\ \overline{\rho}\widetilde{u}_j\widetilde{h}_0-\lambda\frac{\partial \widetilde{T}}{\partial x_j}-\frac{\mu_t}{Pr_t}\frac{\partial \widetilde{h}}{\partial x_j}-\widetilde{u}_i\tau_{ij}\\ \overline{\rho}\widetilde{u}_j\widetilde{k}-\left(\mu+\frac{\mu_t}{\sigma_{k3}}\right)\frac{\partial \widetilde{k}}{\partial x_j}\\ \overline{\rho}\widetilde{u}_j\widetilde{\omega}-\left(\mu+\frac{\mu_t}{\sigma_{\omega 3}}\right)\frac{\partial \widetilde{\omega}}{\partial x_j}\\ \overline{\rho}\widetilde{u}_j\gamma-\left(\mu+\frac{\mu_t}{\sigma_\gamma}\right)\frac{\partial \gamma}{\partial x_j}\\ \overline{\rho}\widetilde{u}_j\widetilde{Re}_{\theta t}-\sigma_{\theta t}\left((\mu+\mu_t)\frac{\partial \widetilde{Re}_{\theta t}}{\partial x_j}\right)\end{bmatrix}\quad \boldsymbol{H}_j$$

$$=\begin{bmatrix}0\\ 0\\ 0\\ P_k+\beta'\overline{\rho}\widetilde{k}\widetilde{\omega}\\ 2\overline{\rho}\frac{1-F_1}{\sigma_{\omega 2}\widetilde{\omega}}\frac{\partial \widetilde{k}}{\partial x_j}\frac{\partial \widetilde{\omega}}{\partial x_j}+P_k\alpha_3\frac{\widetilde{\omega}}{\widetilde{k}}-\overline{\rho}\widetilde{\omega}^2\beta_3P_{\gamma 1}-E_{\gamma 1}+P_{\gamma 2}-E_{\gamma 2}P_{\theta t}\end{bmatrix}$$

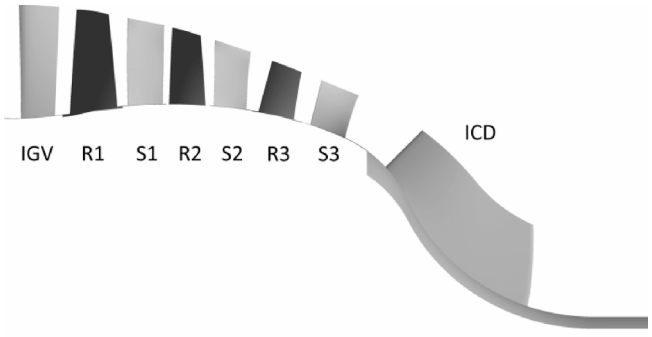

VINK compressor	
Rot. Speed	6242 rpm
Corr. mass flow	91.2 kg/s
PR	2.80
N. stators (IGV, S1, S2, S3, ICD)	76, 88, 93, 91, 8
N. rotors (R1, R2, R3)	51, 69, 72

Fig. 1. Stators and rotors of the VINK compressor and its downstream ICD duct.

The inlet boundary conditions were set using an total pressure of 46,690 Pa, total temperature of 282 K, and turbulence intensity of 5 % [21]. The outlet static pressure was set to 96,000 Pa to reach the correct design total pressure ratio. The various locations of the domain boundaries are shown in Fig. 3. Periodic interfaces were used in the periodic boundaries of each domain while mixing planes connected adjacent domains along the flow path of the compressor.

The CFD approach used in this paper is commonplace in academia and industry for modelling multi-stage turbomachinery but does not account for transient phenomena such as rotor–stator interaction, which can locally impact laminar-turbulent transition. However, the significantly larger computational effort needed for a transient simulation was

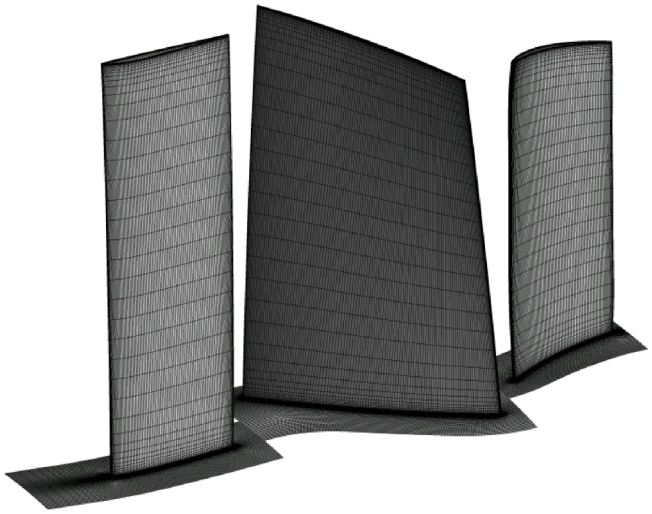

Fig. 2. Surface mesh for the VINK IGV, R1, and S1. The remaining rotors and stators feature similar meshes but have been omitted to improve image clarity.

not warranted since the target of the simulations is to investigate the time-averaged aerothermal performance of the LPC.

The stator surfaces utilize a boundary condition which is representative of a cooling circuit composed of small cooling channels underneath the aerodynamic surfaces (i.e. the stator vane surface, see Fig. 4) where supercritical hydrogen is allowed to flow and pick up heat from the core air stream. For VINK, the flow of hydrogen is split up, routed through cooling channels underneath each stator vane surface, and then mixed back together. The hydrogen mass flow in each cooling channel is assumed to be the same everywhere, which means that the mass flow of hydrogen for each stator depends on its share of the total amount of cooling channels in the VINK compressor.

The cooling channels themselves are assumed to have a square cross-section with a side of 0.5 mm, a spacing of 1.5 mm between each channel, and a 0.5 mm wall thickness for the side facing the core air flow, similar to the cooling channels found in rocket nozzles [28,29]. A circular cross-section could be more beneficial in terms of structural integrity and manufacturing but would also feature less heat transfer area than a square cross-section. The limited heat transfer area was identified previously by Dijk et al [12] to limit the amount of obtainable heat transfer in a stator with circular cooling channels, thereby prompting the use of a square cross-section in this paper. The channels are assumed to be aligned with the span direction of the stators and the number of channels for each stator is calculated using the midspan chord.

The method chosen for modelling the heat transfer from the air to the hydrogen side is based on a thermal resistance which accounts for convection on the air side, conduction in the cooling channel wall, and convection in the cooling channel:

$$R''_{tot} = \frac{1}{h_{conv,air}} + \frac{t}{k} + \frac{1}{h_{conv,H2}} = \frac{1}{U} \tag{2}$$

Here the inverse of the total thermal resistance R''_{tot} is the overall heat transfer coefficient U. In CFX, this was implemented as a boundary condition by using a wall heat transfer coefficient U_{wall} in an equation analogous to Newton's law of cooling, which included the thermal resistance due to conduction in the cooling channel wall, and convection in the cooling channel:

$$q''_x = U_{wall}\left(T_{wall,air} - T_{H2,mid}\right)$$

$$U_{wall} = 1/\left(\frac{t}{k} + \frac{1}{h_{conv,H2}}\right) \tag{3}$$

The air side convective heat transfer as seen in Eq. (2) will be a result of the CFD simulations. These equations assume that the heat transfer through the stator surfaces can be approximated as one-dimensional, accounting for the thickness t of the wall towards to the core air flow and assuming that the heat transfer areas on the hydrogen and air side are of similar magnitude. The wall thickness t between the channel and stator surface was set to 0.5 mm and the thermal conductivity to 120 $\mathrm{W/m\,K}$, which is conservative for Aluminium alloys. It will be shown later in the paper that the total thermal resistance is dominated (80–90 %) by the air side heat transfer coefficient, which means that the overall thermal resistance is relatively insensitive to the assumptions done on the hydrogen cooling channels.

The convective heat transfer coefficient of the hydrogen flow $h_{conv,H2}$ is calculated assuming a fuel-to-air mass ratio of 1 % and a hydrogen inlet pressure and temperature of 42 bar and 100 K, respectively. This corresponds to a hydrogen mass flow of 0.428 $\mathrm{kg/s}$ at the design point of the VINK LPC which is divided equally between all the cooling channels. The chosen inlet temperature of 100 K is meant to maximize the temperature difference between air and hydrogen while avoiding condensation of nitrogen and oxygen in the core air. The temperature $T_{H2,mid}$ in Eq. (3) represents the mid-point of the cooling process along the channels in the individual stators and is used in CFX to calculate the heat flux and for calculating the hydrogen convective heat transfer coefficient $h_{conv,H2}$. The convective heat transfer coefficient for hydrogen has been evaluated using the heat transfer correlation in Eq. (4) by Gnielisnki

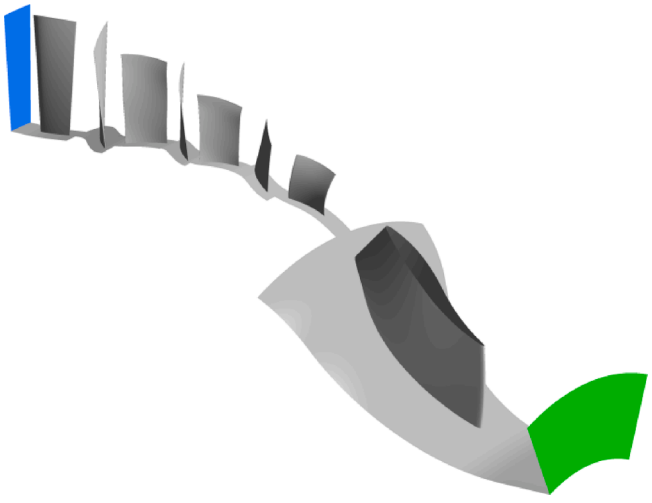

Fig. 3. Domain setup for the VINK compressor. The inlet is marked blue while the outlet is marked green. (For interpretation of the references to colour in this figure legend, the reader is referred to the web version of this article.)

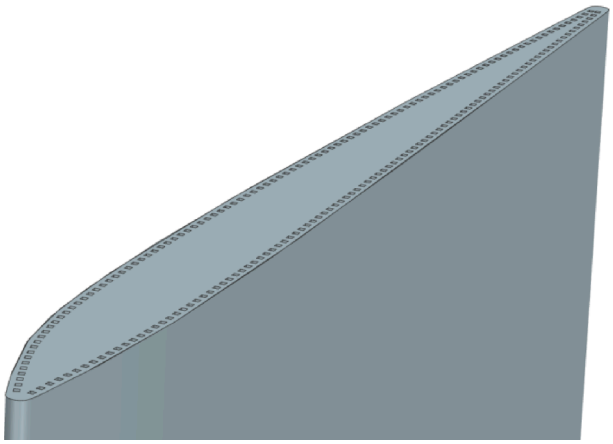

Fig. 4. Cross-section of a generic cooling channel on a vane.

[30], friction factor by Petukhov [31], and real fluid properties from REFPROP [27]. For laminar flow (i.e., $Re < 3000$) the Nusselt number is approximated as 3.66 and the friction factor as $f = 64/Re$.

$$Nu_{H2} = \frac{(f/8)(Re_{H2} - 1000)Pr}{1 + 12.7(f/8)^{1/2}(Pr^{2/3} - 1)} \quad (4)$$

$$f = (0.79\ln Re_{H2} - 1.64)^{-2} (Re_{H2} > 3000) \quad (5)$$

Each stator domain in the CFD model is assumed to constitute its own separate cooling circuit and will therefore have its own distinct heat transfer properties (U and $T_{H2,mid}$). $T_{H2,mid}$ is kept constant at 100 K for the mesh study but will be iterated on for the rest of the cases in order to match the hydrogen temperature rise with the heat transferred through the vane surfaces.

In this study, the obtained hydrogen flow velocities in the cooling channels are relatively low, reaching at most 19 m/s (Mach 0.014), so there is no risk of choking in the cooling channels and the pressure losses in the channels become negligible.

This thermal boundary condition setup allows for modelling the heat transfer occurring inside the vane without explicitly designing and simulating the entire cooling channel geometry in a complex and costly conjugate CFD simulation.

2.3. Experimental facility

The facility, depicted in Fig. 5, is a versatile low-speed compressor rig engineered for continuous operation and a wide operational range. The two-stage compressor drives the main flow and operational conditions are achieved by restricting the flow upstream of the low-pressure compressor and regulating the compressor's input power. The flow is conditioned for thermal and pressure uniformity in a combined volute and flow conditioner. The ICD is mounted downstream of the two-stage compressor and the flow is recirculated for thermal stability, to limit particle ingestion, and for noise mitigation. The facility uses turbulence grids to maintain a base-level turbulence at the inlet of the LPC, operates at atmospheric pressure, and accommodates temperatures between 14 and 21 °C.

The compressor design used in this test facility, shown in Fig. 6, replicates the final stages of the VINK compressor and is used for experimental, computational, and verification purposes. As shown in Fig. 6, this LPC has 75 adjustable inlet guide vanes (IGV), rotor 1 with 61 blades (R1), stator 1 with 124 vanes (S1), rotor 2 with 69 blades (R2), and 126 outlet guide vanes (OGV, S2). The LPC is similar to the two last stages of the VINK LPC, with aerodynamic and geometrical design similarity (Fig. 7) while being constrained by physical and power limitations of the lab and to suitable instrumentation. Even though compressible effects cannot be replicated in this low-speed facility other similitudes such as Reynolds number, tip clearance, turbulence levels, Strouhal number, stacking etc. were carefully selected to achieve predictable and representative flow in the LPC and ICD for maximum measurement accuracy. Further details of the facility and design approach can be found in [18–20].

Instrumentation configuration varies between different tests campaigns. The current study relies heavily on the interface at the inlet of the OGV and outlet of the ICD which are investigated by traversing with several hub mounted traverse systems. A 3 mm multi-hole probe (MHP), 1 mm Kiel probe, and 3 mm hotwire provide total pressure, static pressure, dynamic pressure, flow angles, and turbulence intensity at the traversed interfaces. The static instrumentation and data reduction methods are described in [18]. Noteworthy for the static instrumentation in the current study are the pressure taps on midspan of the OGV which uses a Prandtl tube printed in its leading edge for reference blade loading calculations. The pressure transducers in the facility are PSI-9116, ESP-32HD DTC, FCO432, and FCO-560, which are selected based on the operational conditions and configuration. For hot-wire anemometry a Dantec Constant Temperature Anemometry 56C17 device and a NI-4461 DAQ are chosen which provide instantaneous measurements of velocity, turbulence intensity, and turbulence length scale. All Resistance Temperature Detectors are provided by Pentronic AB following the ISO 17025 accreditation and signals are gathered by a NI-9217 DAQ.

A comparison between numerical and experimental results will be provided in section 3.1 in order to verify the applicability of the CFD setup. The CFD methodology is essentially the same as for the VINK

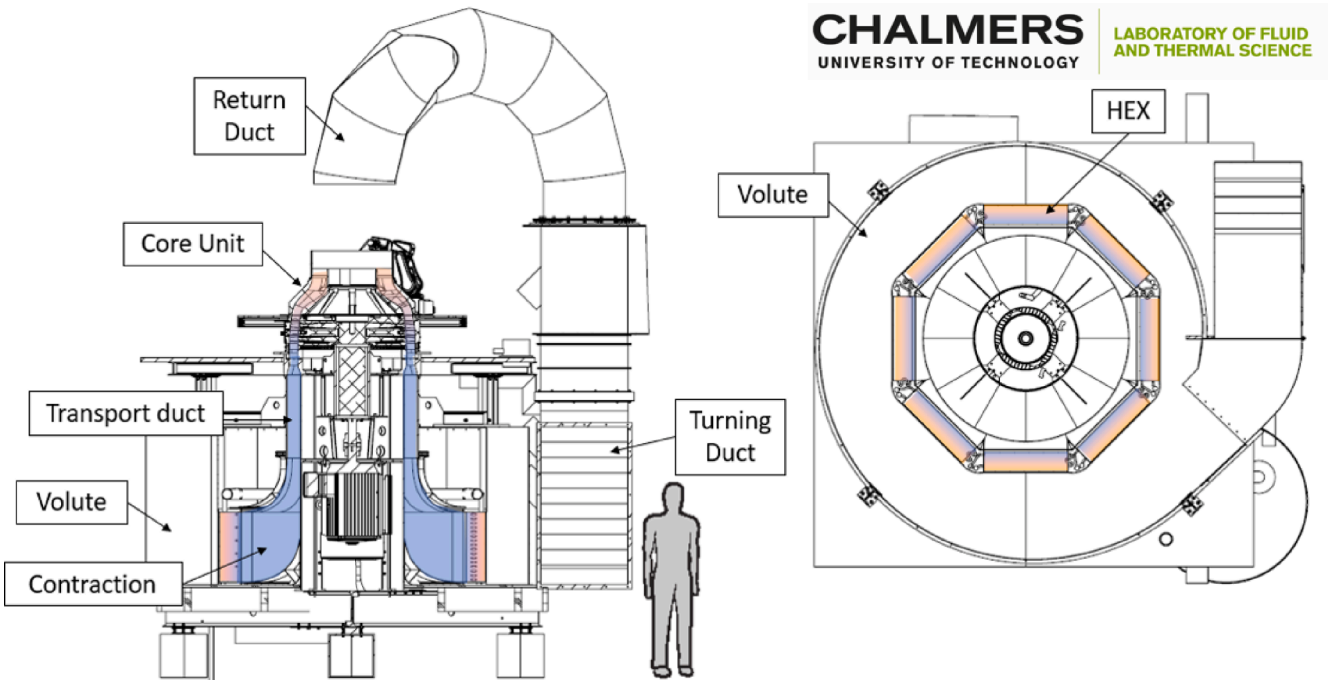

Fig. 5. Schematic representation of the low-pressure compressor facility at Chalmers Fluid and Thermal Science Laboratory: On the left, a vertical section cut with brief descriptions, and on the right, a horizontal section cut at the level of the cooling elements in the volute. Image sourced from [18].

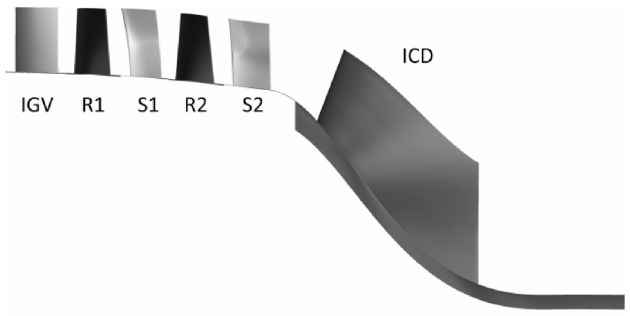

LPC design parameters	
Rot. Speed	1920 rpm
Corr. mass flow	18.4 kg/s
PR	1.07
N. stators (IGV, S1, S2, ICD)	75, 126, 124, 8
N. rotors (R1, R2)	61, 69

Fig. 6. Design parameters of the LPC in the Chalmers low-pressure compressor test facility.

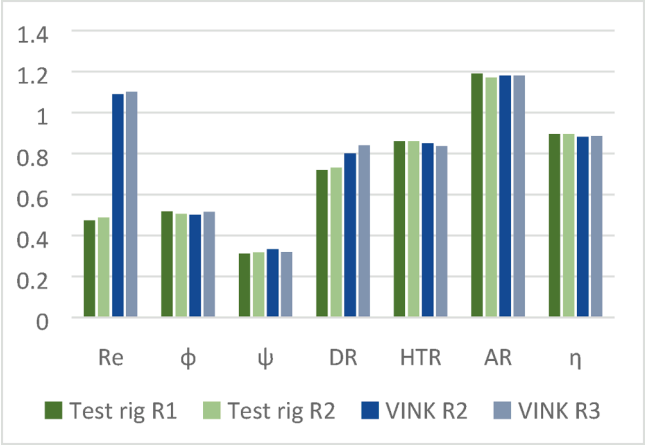

Fig. 7. Aerodynamic and design similarity parameters for the LPC in the Chalmers low-pressure compressor test facility (test rig) in comparison to VINK. AR – Aspect ratio; HTR - Hub-to-tip ratio; DR – Degree of reaction; Re – Chord based Reynolds number, divided by 10^6; ϕ – Flow coefficient; ψ – Stage loading; η_p – Polytropic efficiency.

compressor but with two major differences; it only includes two rotor stages instead of three and all walls are set as adiabatic. The inlet boundary conditions were set using an inlet total pressure of 95,275 Pa, total temperature of 288.15 K and turbulence intensity set to 5 % [21]. The outlet static pressure was set to 100,052 Pa to reach the correct design total pressure ratio.

2.4. System level model

The integrated performance of the proposed intercooler concept is evaluated using Chalmers in-house engine simulation tool GESTPAN (GEneral Stationary and Transient Propulsion ANalysis) [32]. GESTPAN is a generalized simulation system for the prediction of gas turbine performance in design, off-design, and transient conditions. New modules were integrated into GESTPAN to model the performance of hydrogen-fueled propulsion systems, including a dedicated fuel heat management system [6]. Detailed modelling of hydrogen properties with respect to pressure–temperature variations is performed with REFRPOP [27] from cryo-storage up to the combustor inlet condition. Moreover, REFPROP is used to simulate the performance of real compression processes across the various pumps in the fuel system. Combustion is modelled using temperature–pressure and fuel–air-ratio-dependent tables generated using NASA CEA [33]. The tables are generated for a reference fuel temperature and pressure, and therefore the final computed fuel–air ratio for a given turbine inlet temperature or rating is corrected using deviations in fuel enthalpy.

The engine conceptual design is carried out using Chalmers' in-house tool WEICO (WEIght and COst). WEICO allows for estimating turbomachinery stage count, the number and size of compressor blades, using statistical correlations for stage loading, diffusion factor, hub-to-tip ratio, and aspect ratio. The increase in core specific power as a result of intercooling is expected to impact the turbomachinery size. Therefore, corrections are applied to the polytropic efficiency using the last stage blade height in equation (6) [34].

$$\eta_{p,\mathrm{HPC}} = \eta_{p,0,\mathrm{HPC}} + \Pi\left(0.0532 - \frac{0.5547}{\lambda} - \frac{1.7724}{\lambda^2}\right) \tag{6}$$

Where λ is the last blade height in mm and Π is a correction factor assumed to be equal to 1 for the HPC and 0.5 for the high-pressure turbine (HPT). For calculating the last blade height an HPC exit hub-to-tip ratio of 0.92 and axial Mach number of 0.27 are assumed [34]. The high-pressure compressor efficiency is expected to be impacted by the height of the last stage blade height. Values of hub-to-tip ratio larger than 0.92 are known to result in smaller blades and increase in tip-leakage and endwall losses. The value of 0.27 in axial Mach number is typically found in the last stages of the high pressure compressor and was chosen for the present study.

Intercooling impacts NOx emissions by reducing the HPC outlet temperature. In the present paper the Emission Index of NOx (EINOx) is estimated for a micromix combustor using the correlation for dry air derived in the ENABLEH2 project [35]:

$$EINOx = 0.0864\, p_3^{0.4} e^{T_3/191} \phi^{1.95} \quad [\mathrm{g/kg}]\mathrm{fuel} \tag{7}$$

In the equation above p_3 is the HPC delivery pressure in kPa and ϕ is the equivalence ratio. It should be noted that the EINOx correlation Eq. (7) was derived for a constant fuel temperature of 450 K. Hence, Eq. (7) does not include the effect of varying fuel temperature. Therefore, T_3 is corrected to include the impact of fuel temperature by assuming adiabatic mixing at constant pressure:

$$T_3 = T_{H2}\frac{c_{p_{H2}}\dot{m}_{H2}}{c_{p_{air}}\dot{m}_{air} + c_{p_{H2}}\dot{m}_{H2}} + T_{air}\frac{c_{p_{air}}\dot{m}_{air}}{c_{p_{air}}\dot{m}_{air} + c_{p_{H2}}\dot{m}_{H2}} \tag{8}$$

where T_3 is the fuel–air mixture temperature, in K.

The heat transfer performance of the integrated intercooler concept is modelled using the plate correlations available from literature (Incropera et al.) [36] for the average Nusselt number $\overline{Nu}_L$, assuming mixed flow (laminar and turbulent):

$$\overline{Nu}_L = \left(\frac{T_{wall,air}}{T_{\infty,air}}\right)^{-n}\left(0.037 Re_L^{0.8} - A\right) Pr^{1/3} \tag{9}$$

$$A = 0.037 Re_{crit}^{0.8} - 0.664 Re_{crit}^{1/2}$$

The first term in equation (9) represents the temperature correction factor to account for large temperature variations in the boundary layer, where the exponent n can vary between 0.25 and 0.4 [37]. Here $n = 0.25$ is used. The parameter A is used to represent the mixed flow condition, where the critical Reynolds number, Re_{crit} varies with the turbulence intensity, Tu, using the following expression [37]:

$$Re_{crit} = \sigma\left(3.6 \times 10^5\right)\left(100 \cdot Tu\right)^{-5/4} \tag{10}$$

It should however be noted that the following correlation is an oversimplification of the transition phenomena in compressor vanes. First, the boundary development behaves differently depending on which side of the airfoil is being considered, with the suction side

behavior being more difficult to predict and therefore more critical to determine the correct vane heat transfer performance. Second, the proposed correlation is only valid for a bypass mode transition [38], whereas a compressor can also experience separated-flow mode transition. It is also highly dependent on the compressor design and operation mode. For example, controlled diffusion designs strive to achieve laminar flow prior to the point of minimum pressure and to promote turbulent flow immediately after. In this way, the largest diffusion takes place on the turbulent side and the flow is least likely to separate. At the same time the laminar flow allows for reducing the profile losses. The aforementioned reasons make it hard to select the most accurate model to predict the onset of transition at a system level. Still, neglecting transition, might lead to unreasonably high levels of heat transfer, in particular for smaller engines operating at moderate to low Reynolds numbers. Therefore, the present paper includes a CFD study on transition in compressor blades from which the turbulence intensity levels are going to be extracted and the Re_{crit} is going to be calibrated using the proposed σ factor. As will be demonstrated in section 3.2.3, this approach gives reasonable results when applied to a specific compressor design, size and operation. It should not be employed outside the conditions specified in the present paper.

The heat transfer performance in the hydrogen cooling channels is modelled using the same Nusselt number correlations and flow friction factors as was specified in Eq. (4) and (5). For the estimation of Reynolds and Prandtl numbers the properties are averaged at the mid-point temperature between the inlet and outlet of the heat-exchanger [39]. This approximation, although valid for the temperature ranges employed in the present paper, should be used with care when applied to larger temperature variations and/or when the variation takes place close to the critical point. The final performance of the heat-exchanger is calculated using the ϵ-NTU method for a crossflow single-pass heat-exchanger with both fluids unmixed:

$$\epsilon = 1 - \exp\left(\frac{NTU^{0.22}}{C_r}\left[\exp\left(-C_r \cdot NTU^{0.78}\right) - 1\right]\right) \tag{11}$$

Where $C_r = C_{min}/C_{max}$, ϵ is the effectiveness, and $NTU = UA/C_{min}$ are the number of transfer units. The heat capacity rates C_{min} and C_{max} are evaluated for the hydrogen and air sides, respectively. Due to the large differences in mass flow the minimum heat capacity rate was always connected to the hydrogen side in the present study. The overall heat-transfer coefficient, U, times the heat-exchange area, A, is:

$$UA = \frac{A}{\frac{1}{h_{conv,air}} + \frac{t}{k} + \frac{1}{h_{conv,H2}}} \tag{12}$$

Here t is the wall thickness between the air side surface and the inner cooling channel surface. Hence, any two-dimensional thermal resistance effects related to tube interspacing are neglected in the present study. The thermal resistance of the material is defined by k. It is also assumed that the effective heat-exchange area, A, is the same on both sides of the heat-exchanger and that it is defined by the air-side wetted area of the vane. Both assumptions are not expected to have a large influence on the results since the thermal resistance is dominated by the much higher thermal resistance on the air side, from which the heat-transfer area was defined.

3. Results

This section of the paper will start with the experimental validation of the CFD methodology, followed by an assessment of the heat transfer potential for VINK, where the cooled VINK compressor will be analyzed, and its performance discussed. The effect of fully turbulent or transitional flow on heat transfer will be investigated, as well as comparisons between CFD and heat transfer correlations from literature to support the system level engine performance calculations which conclude this section.

3.1. CFD validation

A mesh study was carried out for the LPC in the low-speed compressor test facility where the overall cell count was varied between 4.8 and 16 million cells while monitoring the change in pressure ratio, mass flow and polytropic efficiency. The largest difference in the monitored properties was for the mass flow which differed by 0.5 % when comparing the finest and coarsest mesh grids. The cell count of the final, chosen mesh totaled approximately 8 million cells and constitutes a reasonable balance in terms of computational cost and accuracy.

The LPC was numerically modelled using mixing planes which average out tangential variations such as wakes from upstream stators and rotors. Experimental data radial profiles were hence averaged similarly by using 600 points covering a sector of five of the S1 stators.

A comparison is shown in Fig. 8 between experiments and CFD for the normalized total pressure as function of radius at the OGV inlet, demonstrating a good agreement between numerical and experimental results. The tangentially averaged boundary layer matches well with experiments from 90 % of span and above, except at the last experimental point where CFD predicts a higher total pressure. The radial profile shows good agreement with experiment from 40 % of span and below, with only minor variation. However, between 40 and 80 % of span, the CFD simulation predicts higher total pressure relative to the experimental measurement, while a lower total pressure is observed between 80 and 90 % of span.

In Fig. 9, the dynamic pressure at the OGV inlet is illustrated with CFD simulations shown in blue and MHP readings in black. Acceptable general trends between experimental data are evident, considering potential interference in MHP data from pressure gradients [40,41] and angle fluctuations [42].

Fig. 10 compares the pressure distribution on the OGV, instrumented with midspan pressure taps, with CFD simulations at design conditions. Using experimental operational conditions, the numerical simulation (solid blue line) satisfactorily matches the blade loading of the LPC numerical model.

A comparison of normalized total pressure contours at the ICD outlet at 50 % of design rotational speed (referred to as N0.5-ADP) is depicted in Fig. 11. CFD results are on the left, and experimental data on the right. A general agreement exists between the numerical and experimental results at the ICD outlet. The corner vortices at the hub/strut intersection are similar, especially the left corner vortex which is of comparable size and position when comparing CFD to experimental results. The right corner vortex on the other hand, is located closer to the hub in the experiments than in the CFD results. Near the shroud, above 90 % of span,

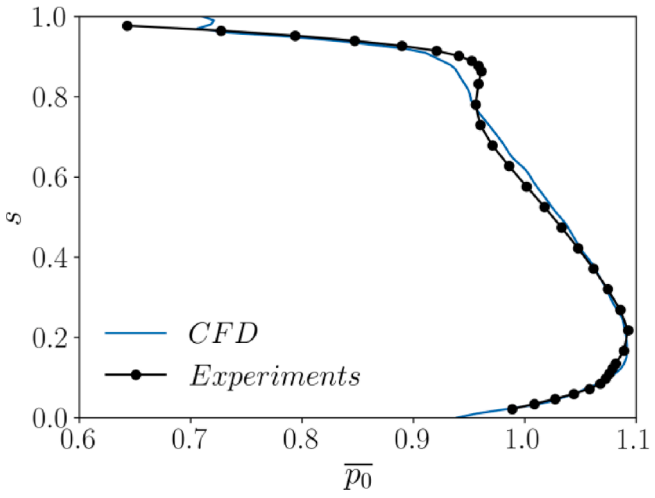

Fig. 8. Normalized total pressure along the span s at the inlet of the OGV for the Kiel probe measurements and CFD simulations.

one can observe a low momentum flow with distribution similar to the experimental results, exhibited by a slight downward distribution where the strut interacts with the shroud boundary layer.

Fig. 12 displays normalized total pressure at the same rotational speed as N0.5-ADP but with a higher pressure ratio (+25 %), with numerical results on the left and experimental results on the right. The numerical results generally agree with the experimental data, although secondary flow structures from the hub/strut are found at a higher radial position in the numerical results compared to the experimental results. Near the shroud, the numerical results overpredict the boundary layer thickness, but the stator/shroud interaction is predicted accurately.

3.2. VINK compressor heat transfer potential

3.2.1. Mesh study results

For the VINK compressor the overall mesh cell count was varied between 4 and 32 million cells while monitoring the change in pressure ratio, mass flow, polytropic efficiency, and heat flow, the last of which was modeled using the approach presented in Eq. (3). Fig. 13 shows the values of these properties as function of mesh cell count, in proportion to the finest mesh at 32 million cells. The largest difference in the monitored properties of the mesh study was found for the heat flow, amounting to at most 1 % compared to the finest mesh. The remaining properties featured even smaller differences among the analyzed computational meshes. From the figure it can be seen that the 8 million cell mesh is a good compromise between computational cost and accuracy and was therefore chosen for subsequent CFD simulations of the VINK compressor.

3.2.2. Aerothermal performance

The cooling of the flow in the VINK compressor has led to a minor change in operating point; the pressure ratio has decreased from 2.8 to 2.79 while the corrected mass flow has increased from 91.2 to 92 [kg/s]. The boundary condition representing the hydrogen heat transfer was iterated on until no appreciable change was found in the hydrogen bulk temperature $T_{mid,H2}$ inside the cooling channels and is shown in Table 1. The heat transfer coefficients U_{wall} for each stator are relatively similar and only changed by a few percent during the iterations carried out.

Table 2 shows the total pressure loss coefficient $\xi = (p_{0,in} - p_{0,out})/p_{dyn,in}$ which has seen decreases for all stators compared to the baseline case (6.8 to 24 % decrease) except for stator S1, which has experienced an increase of 3.3 %. The loss composition of a compressor stage is typically considered to consist of viscous losses, shock losses, endwall losses, and tip leakage losses [43]. For a multistage machine,

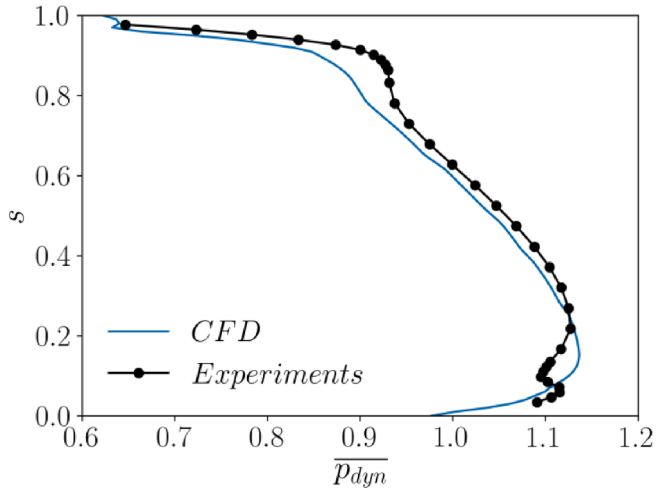

Fig. 9. The dynamic pressure along the span s at the inlet of the OGV from MHP measurements and CFD.

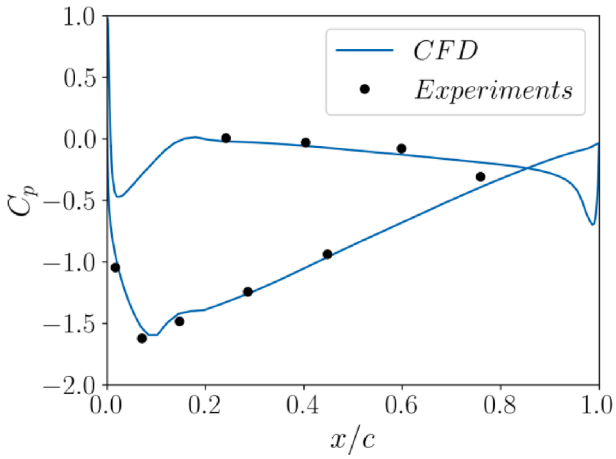

Fig. 10. Blade loading at midspan for the OGV as function of normalized streamwise distance.

complexity increases further since the loss composition is also dependent on the flow and losses in upstream components. A comprehensive, fully detailed analysis of the loss composition in the cooled VINK compressor is outside the scope of this paper, and would merit its own, separate paper. Nevertheless, there are some immediate insights which can be gained by looking at the stator with the largest reduction in total pressure loss coefficient, stator S3. As stated earlier, the pressure loss coefficient has decreased by 24 % for this component. The first loss to investigate ought to be the viscous losses since these often account for roughly half of the overall losses [38]. This is illustrated in Fig. 14a) in terms of wall shear stress at midspan and shows that the cooled S3 vane actually features higher wall shear stress than the un-cooled baseline S3 vane, contrary to the change in total pressure loss coefficient. Although not shown here, this behavior in wall shear stress extends to rest of the span locations in the vane. When analyzing the radial profile of the total pressure loss coefficient Fig. 14b) and Mach number contour in Fig. 15 it becomes more evident that the decrease in total pressure loss coefficient is due to the extent of the separated region on the suction side of the vane, which starts near the trailing edge. This phenomenon has been encountered in similar research on cooled compressor vanes [16] and is a result of the cooling resulting in a thinner boundary layer compared to the uncooled case. This leads to higher shear stresses due to the higher velocity gradients and increases turbulent mixing which delays the turbulent separation.

This operating point of the compressor leads to a net reduction in total pressure coefficient for the S3 stator due to the separation near the trailing edge. A different operating point (or redesigned stator) where the flow remains attached could instead lead to an increased total pressure loss for the cooled stator. Ultimately, a future design update of the VINK compressor should include the effects of heat transfer in addition to common compressor trade-offs in terms of efficiency and surge margin, thereby accounting for the effects of cooling on the flow and to maximize heat transfer. Nevertheless, the results here show that cooling can be achieved without incurring a major penalty in terms of total pressure loss, even before carrying out additional aerodynamic optimization and reshaping.

The heat transfer on the air side has been summarized in Table 2 and shows that the overall heat flow reached 403 kW, an equivalent 9.4 K core air temperature drop, and a hydrogen temperature increase of 59 K. S3 is responsible for the largest share of the heat flow and also features the highest average convective heat transfer coefficient. Fig. 16 shows the obtained wall temperatures for the VINK compressor where the lowest average surface temperatures can be found in the IGV. The hydrogen mass flow was assumed to be divided equally between each cooling channel in each stator but could be adjusted in a future design update to prevent cold spots or in order to maximize the overall heat

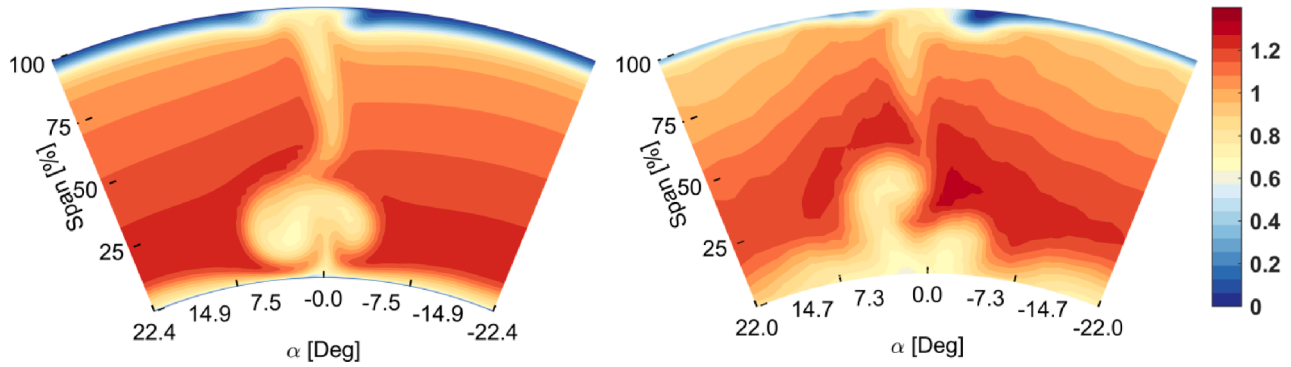

Fig. 11. Normalized total pressure contours at the outlet plane at N0.5-ADP: CFD simulation (left) and experimental data (right).

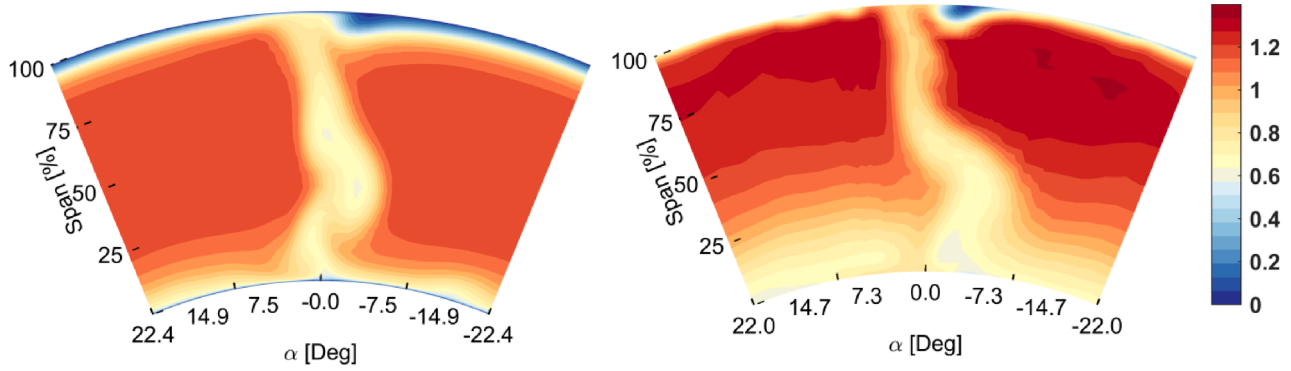

Fig. 12. Normalized total pressure contours for the operational conditions at N0.5-ADP with + 25 % pressure ratio at the outlet: CFD simulation (left) and experimental data (right).

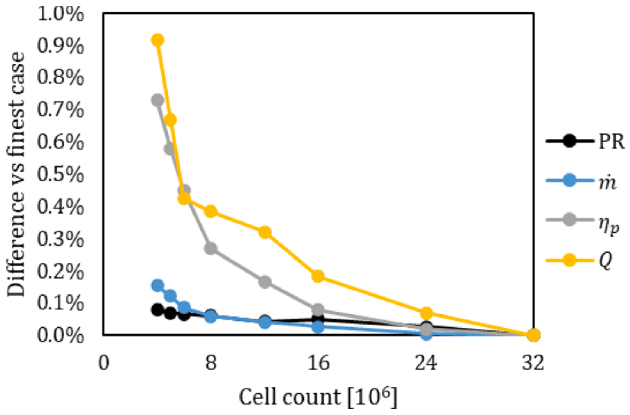

Fig. 13. Mesh study results.

Table 1
Hydrogen cooling channel heat transfer properties.

	IGV	S1	S2	S3	ICD
$T_{mid,H2}$ [K]	122.4	127.3	131.0	132.0	137.5
Re_{H2}	6296	6152	6048	6015	5881
Nu_{H2}	28.57	20.14	19.82	19.73	19.32
$h_{conv,H2}$ [W/m²K]	4529	4611	4667	4684	4751
U_{wall} [W/m²K]	4445	4524	4578	4595	4658

flow. Currently, the coolant flows through the vanes in a crossflow configuration, but there is a possibility to route it in a counterflow manner as well (ICD → S3 → S2 → S1 → IGV), which would lead to higher hydrogen bulk temperatures and wall temperatures at the IGV.

The total thermal resistance R_{tot} in Eq. (2) is dominated by the air side heat transfer coefficient, accounting for roughly 80–90 % of the thermal resistance, while the remainder is due to the contribution from the hydrogen convective heat transfer. The contribution from conduction in the cooling channels is in the order of half a percent due to the thin wall geometries and high thermal conductivity of the material. Decreasing the thermal conductivity by a factor of 10, e.g., using steel or titanium alloy Ti-6Al-4 V, or increasing the wall thickness by the same factor only increases the share of conduction to 2–3 % of the overall thermal resistance, meaning that changing the structural material of the vane does not have a large impact on the performance of this cooling channel design. The low heat exchanger effectiveness for this design is on the other hand indicative of a need for more heat transfer surface area on the air side.

3.2.3. Comparison with empirical correlations

A comparison with an empirical correlation from literature [36] has been carried out in which the air side local convective heat transfer coefficient at midspan is calculated using the following correlation:

$$Nu_x = \left(\frac{T_{wall,air}}{T_{\infty,air}}\right)^{-n} 0.0296 Re_x^{4/5} Pr^{1/3} \tag{13}$$

This correlation is valid for turbulent flow over flat plates and is corrected with the same temperature ratio as was used in (9). The value of the exponent was set to 0.25 since it provides the best fit against the presented CFD data. The Reynolds number in Eq. (13) has been evaluated using the axial velocity at the inlet of each stator, thereby assuming that the swirl component present in the flow should not be considered part of the average "freestream" velocity since it is mostly converted into static pressure in the stator. The results provided by the correlation are shown in Fig. 17 and agree well with CFD, except for regions close to the leading and trailing edges where the surface curvature is the highest.

Table 2
Heat transfer results for the cooled VINK compressor, using the fully turbulent model. The midspan Reynolds number has been evaluated using the axial inlet velocity of each stator.

Overall heat transfer	
Overall heat flow Q[kW]	403
Overall surface area $[m^2]$	4.07
Overall H2 temperature increase $\Delta T_{0,H2}$[K]	58.7
Equivalent core air temperature drop $\Delta T_{0,air}$[K]	9.4
IGV	
Heat flow Q_{IGV}[kW]	57.4
Effectiveness	24.6 %
ξ difference relative to uncooled baseline	−9.4 %
Surface area $[m^2]$	1.18
Midspan chord Reynolds number Re_c	$2.40{\cdot}10^5$
Ave. heat transfer coefficient $h_{conv,air}$ $[W/m^2K]$	334
S1	
Heat flow Q_{S1}[kW]	91.0
Effectiveness	25.2 %
ξ difference relative to uncooled baseline	+3.3 %
Surface area $[m^2]$	1.11
Midspan chord Reynolds number Re_c	$3.20{\cdot}10^5$
Ave. heat transfer coefficient $h_{conv,air}$ $[W/m^2K]$	492
S2	
Heat flow Q_{S2}[kW]	100
Effectiveness	24.5 %
ξ difference relative to uncooled baseline	−10 %
Surface area $[m^2]$	0.810
Midspan chord Reynolds number Re_c	$3{,}69{\cdot}10^5$
Ave. heat transfer coefficient $h_{conv,air}$ $[W/m^2K]$	655
S3	
Heat flow Q_{S3}[kW]	105
Effectiveness	22.3 %
ξ difference relative to uncooled baseline	−24 %
Surface area $[m^2]$	0.605
Midspan chord Reynolds number Re_c	$5.22{\cdot}10^5$
Ave. heat transfer coefficient $h_{conv,air}$ $[W/m^2K]$	826
ICD	
Heat flow Q_{ICD}[kW]	49.9
Effectiveness	26.3 %
ξ difference relative to uncooled baseline	−6.8 %
Surface area $[m^2]$	0.366
Midspan chord Reynolds number Re_c	$2.29{\cdot}10^6$
Ave. heat transfer coefficient $h_{conv,air}$ $[W/m^2K]$	636

There is also a region on the S3 suction side (SS) where the correlation differs a bit compared to CFD due to high flow velocities, reaching slightly above sonic speeds.

Transition is known to play an important role in the flow in gas turbines and for compressors it usually manifests itself in terms of bypass transition or transition induced from separated flow [38]. Transition will also have an effect on heat transfer since the part of an airfoil with laminar flow experiences lower heat transfer coefficients than if it was fully turbulent. A common rule-of-thumb [38] suggests that transition occurs at a Reynolds number based on the streamwise distance of about 350,000, but this depends on several factors such as freestream turbulence levels, pressure gradient, and surface curvature. Therefore, in order to assess the impact of transition on heat transfer the two-equation Gamma-Theta transition model was included into the existing CFD model.

With transition the overall heat flow has decreased from 403 kW to 340 kW, with the IGV experiencing the largest drop in heat transfer (35 %) while ICD only decreasing by 3 %. For this case with transition the heat transfer correlations published by Lienhard [37] were used to provide a comparison with CFD:

$$Nu_x = \left(Nu_{lam}^5 + \left(Nu_{trans}^{-10} + Nu_{turb}^{-10}\right)^{-1/2}\right)^{1/5} \tag{14}$$

$$Nu_{lam} = 0.332 Re_x^{1/2} Pr^{1/3} \tag{15}$$

$$Nu_{trans} = 0.332 Re_{crit}^{1/2} Pr^{1/3} \left(\frac{Re_x}{Re_{crit}}\right)^c$$

$$c = 0.9922 \log_{10}(Re_{crit} - 3.013)$$

$$Re_{crit} = \sigma\left(3.6{\cdot}10^5\right)(100Tu)^{-5/4} \tag{16}$$

The turbulent Nusselt number is calculated using Eq. (13) and uses 1/3 as the exponent for the Prandtl number instead of the 0.6 suggested by Lienhard, which makes it more consistent with the fully turbulent correlations used earlier. The equation for Re_{crit} also includes a scaling factor σ for better matching the location of the critical Reynolds number with the CFD results. A value of 1.75 was used for this parameter, which is less than the factor of 2 which Lienhard suggested to cover the experimental data in his paper [37]. The turbulence intensity Tu used in this expression has been set to 2.5 %, which was the average for all stators in the CFD simulation and will also be used in the system level performance analysis later in this paper.

The comparison between CFD and correlation is shown in Fig. 18. For the suction sides of the stators there is good correspondence between CFD and the correlation used, even though there are some differences in the location and slope of the transition region, especially for the IGV. Also, the pressure side of the IGV remains fully laminar contrary to what is suggested by the correlation, possibly due to the acceleration of the

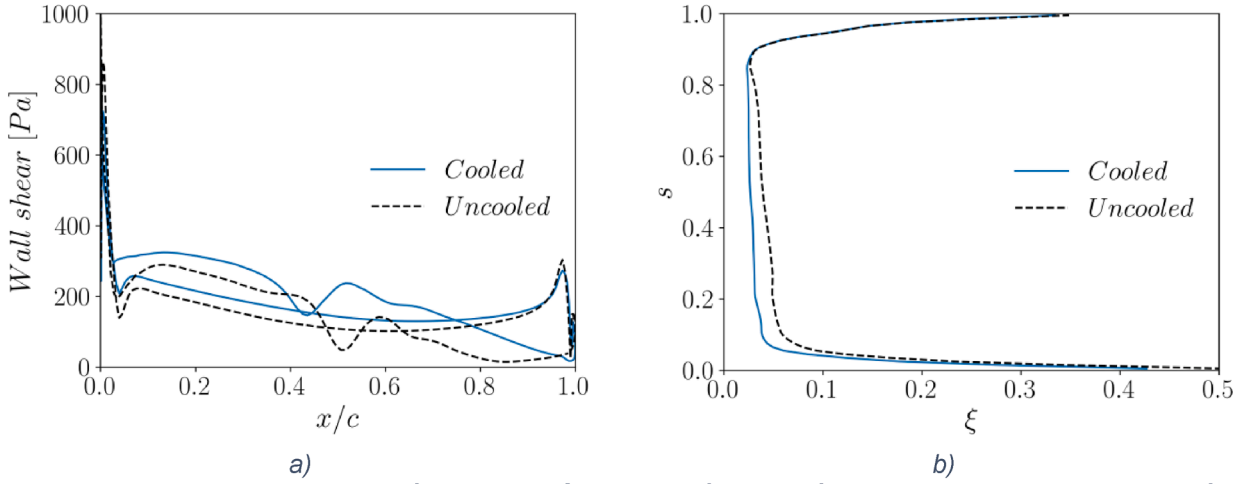

Fig. 14. A) wall shear at midspan for the vink s3 stator as function of normalized streamwise distance for the cooled and un-cooled (baseline) case. b) total pressure loss coefficient $\xi = (p_{0.in} - p_{0.out})/p_{dyn.in}$ as function of span at the S3 outlet. Both cases are treated as fully turbulent.

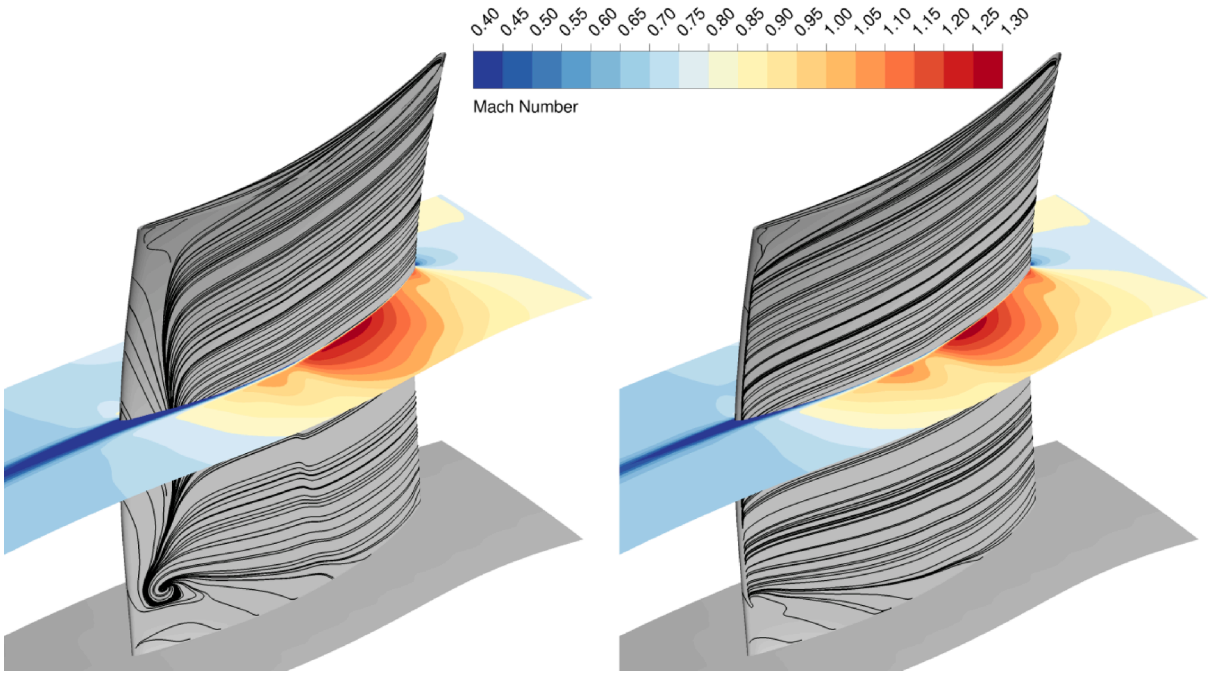

Fig. 15. Mach number contours at midspan for the S3 stator, uncooled case to the left, cooled case to the right. Surface streamlines are projected onto the suction side of the vane. Flow goes from right to left. Both cases are treated as fully turbulent.

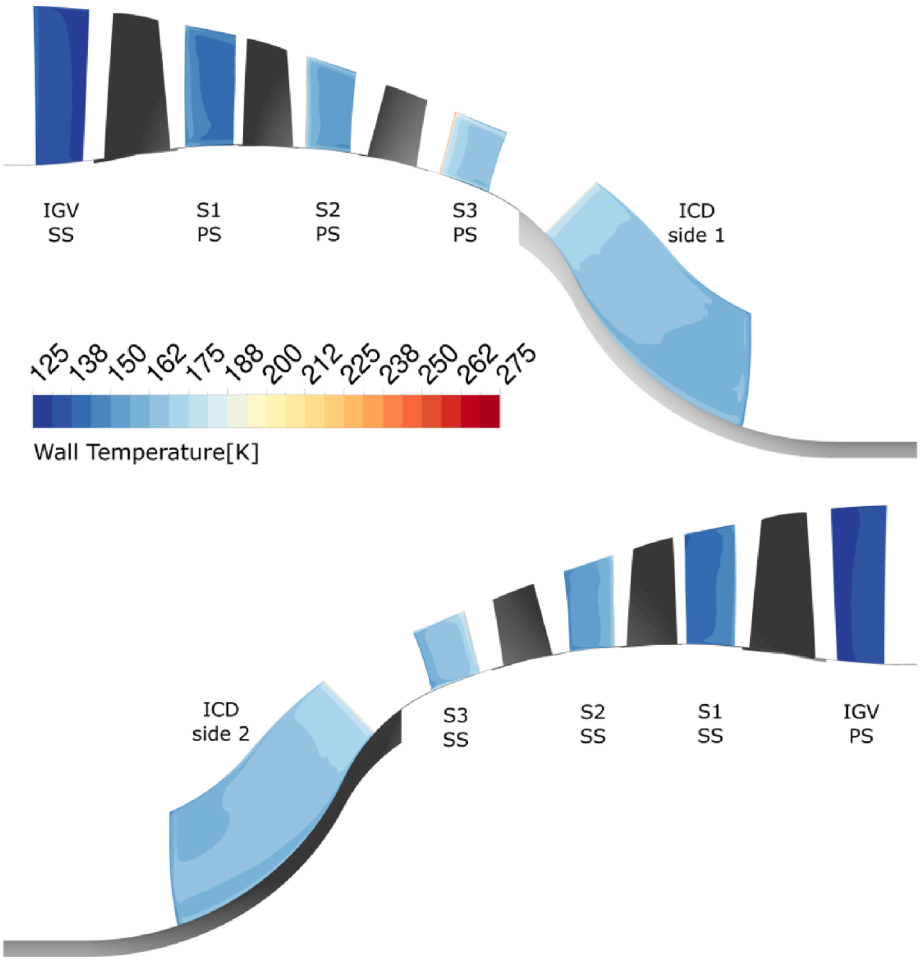

Fig. 16. Wall temperatures for the stator surfaces in the VINK compressor, computed with the fully turbulent model. The ICD does not feature a distinct pressure and suction side since it produces no flow turning and its inflow is almost perfectly axial. Therefore, side 1 and 2 have been used as the naming convention.

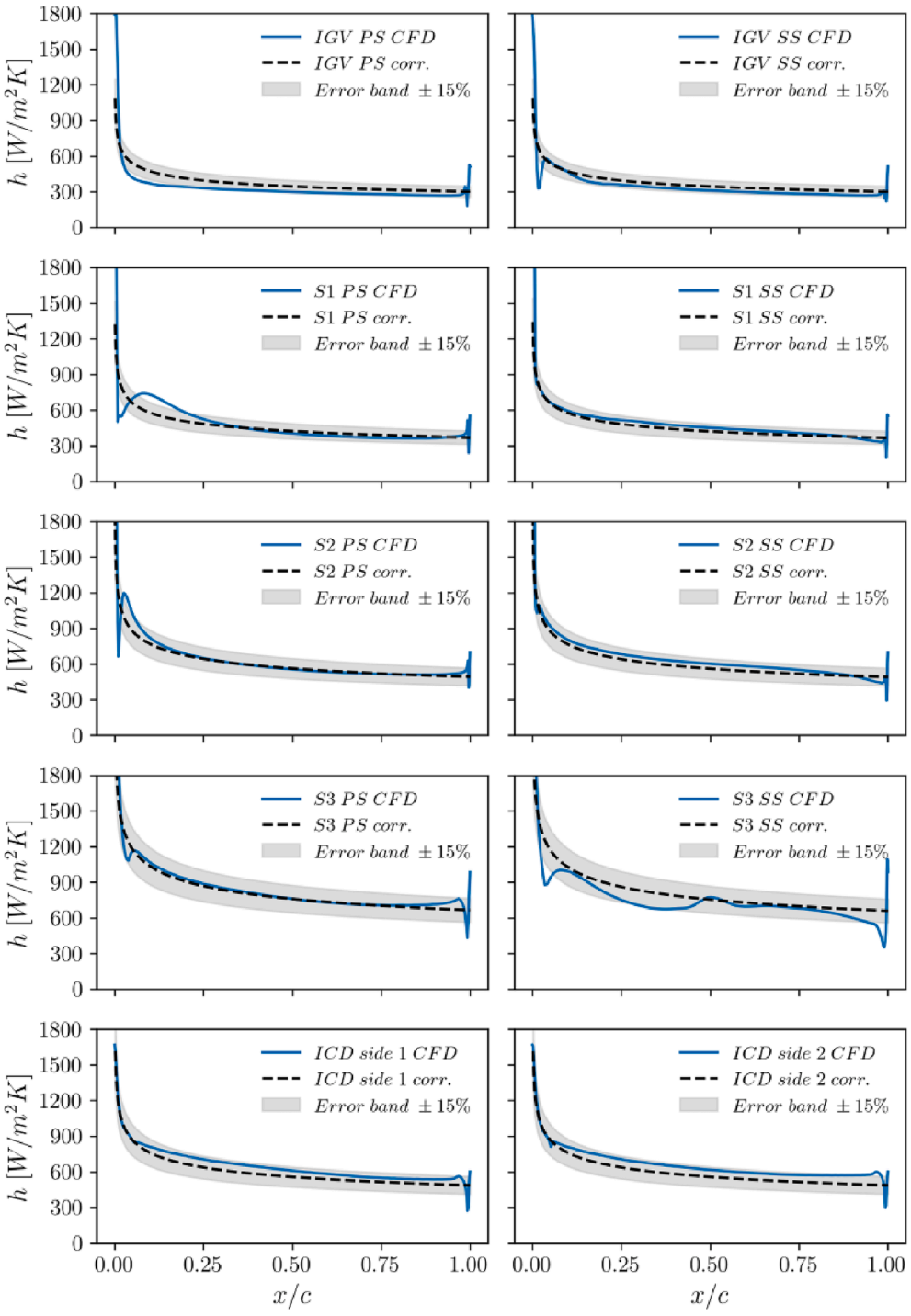

Fig. 17. Heat transfer coefficient as function of normalized streamwise distance at the midspan position of the VINK stator blades. The solid blue line represents values from CFD (fully turbulent) while the dashed line represents values calculated from the flat plate correlation in Eq. (13). The grey band corresponds to a ± 15 % error level for the correlation. (For interpretation of the references to colour in this figure legend, the reader is referred to the web version of this article.)

boundary layer in this side of the blade. The pressure side of S3 is also well-matched by the correlation while the S1 and S2 pressure sides differ in the first halves of the airfoils due to laminar flow separation near their leading edges. This separation then re-attaches as a turbulent boundary layer as shown for stator S1 in Fig. 19.

The correlation (Eq. (9)) used in the system level performance analysis has been compared to the average heat transfer coefficients from CFD and to the correlation by Lienhard (Eq. (14)) to assess its accuracy and suitability. Here the values from the CFD simulation are area-averaged for each stator pressure and suction surface, while the correlations are evaluated at midspan. The results are shown in Fig. 20 and correspond to what was found in Fig. 18, namely that the largest differences compared to CFD are found for the IGV pressure side (PS) (25 %), S1 PS (43 %), and S2 PS (38 %). For the remaining locations, where the flow has not separated nor remained laminar, the difference in heat transfer coefficient between Eq. (9) and the CFD ranges from 1 % to 17 %. Therefore, the correlation yields decent accuracy as long as the flow remains attached, and that transition is dominated by the bypass mode.

In conclusion, if this compressor can be designed to operate as fully

turbulent then the heat transfer can be increased by approximately 20 % compared to the case with transition. This comes at a price of increased pressure drop compared to the transitional case (Table 3), which is largest for the IGV and amounts to a 29 % increase in total pressure loss coefficient compared to the transitional case.

3.3. System level performance

The cooling channel concept is going to be further evaluated regarding its impact on the whole engine performance. More specifically, the usage of the low-pressure compressor stator vanes for the purpose of intercooling is simulated on a large geared turbofan engine in the 84,000 lbf thrust class for long range applications with EIS in 2050. The three-stage low-pressure compressor static components (IGV, S1, S2, S3) will be used to pre-heat the fuel, which is assumed to be evenly split between the vanes. For this particular application 25 % of the H2 fuel goes through each row of vanes and it is evenly split between the inner channels. The inner channels are dimensioned to operate under turbulent flow with acceptable inner H2 pressure losses. The flow on the air-side is assumed to be mixed for which the critical Reynolds number is

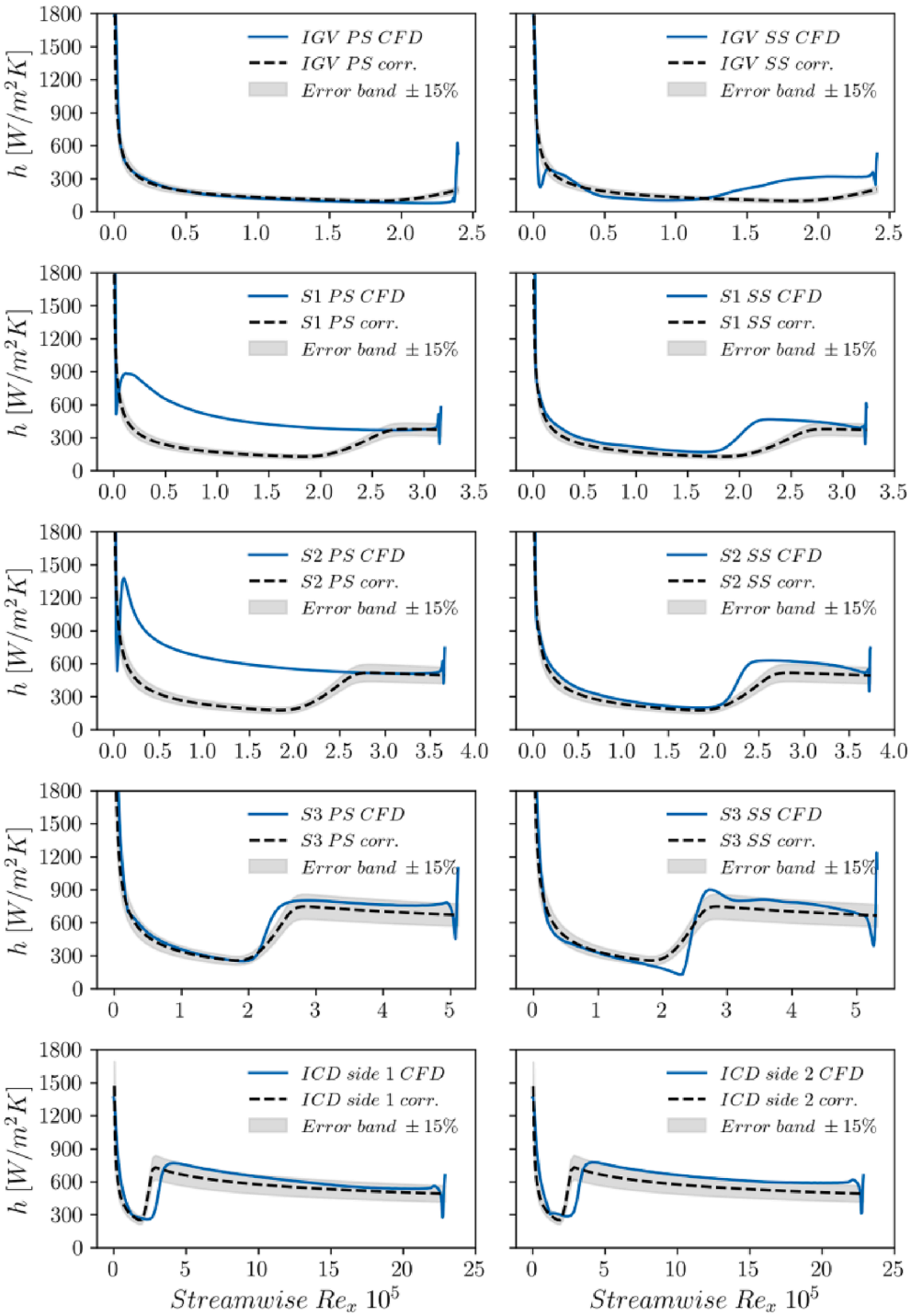

Fig. 18. Heat transfer coefficient as function of streamwise distance Reynolds number Re_x at the midspan position of the VINK stator blades. The solid blue line represents values from CFD (with transition model) while the dashed line represents values calculated from flat plate correlations with transition. (For interpretation of the references to colour in this figure legend, the reader is referred to the web version of this article.)

calculated using eq. (10) with the turbulent intensity and calibration factor provided by the CFD computations in section 3.2.3. It is noted that the VINK compressor geometry presented in section 2.1 is of similar size and type of the conceptual design used in the performance study, hence it assumed to behave similarly with respect to aerothermal performance. The vanes are assumed to be fabricated out of aluminum with a thermal conductivity equal to $k = 120\mathrm{W/m\,K}$, similar to aluminum 2219.

The technology parameters used to establish component performance at cruise conditions in the notional year 2050 geared turbofan engine are listed in Table 4.

The engine conceptual design is carried out using Chalmers' in-house tool WEICO from which a cross-sectional drawing is provided in Fig. 21. The architecture comprises the three-stage low-pressure compressor, a ten-stage HPC, a two-stage HPT and a three-stage low-pressure turbine (LPT). The fan tip diameter at the inlet is 3.2 m, and the last stage blade height of the high-pressure compressor is about 15 mm for the baseline engine (i.e., without intercooling). The baseline engine weight including nacelle is 9518 kg.

A comparison between the baseline and intercooled engine performances is listed in Table 5. The baseline cycle performance is mostly retained, and the low-pressure system is rematched to the new core by increasing the bypass ratio (BPR) and keeping the fan pressure ratio constant until the same velocity ratio (V18/V8) (V18 – cold exhaust velocity, V8 – hot exhaust velocity) is achieved. The obvious differences, relative to the baseline cycle, is a decrease in HPC outlet temperature due to the reduction of core air temperature in the intercooler, increase in BPR due to an increase in core specific power, and an increase in fuel temperature due to the pre-heating of fuel in the intercooler. Specific fuel consumption is therefore mainly affected by a change in fuel enthalpy due to pre-heating. In general, for the proposed design we see a net reduction in SFC, although marginal (0.8 % in cruise) due to the low amounts of enthalpy recovered into the fuel in the intercooler. One might argue that this analysis does not allow to fully quantify the potential of intercooling on cycle performance. Intercooling allows for reduced temperatures at similar overall pressure ratio (OPR) levels, opening for the possibility of further increasing the pressure ratio until temperature limitations or scale effects on component efficiencies deny further improvements. This was not addressed in the present paper. On the other side, it is observed that NOx emissions are reduced due to intercooling if the cycle OPR is left unchanged. Again, the variations are quite small since for the proposed cooling concept the limited core temperature drop only allows for EINOx reductions of 6.3 % at take-off down to 3.6 % at cruise. The uncertainty margins of -+15 % associated with the Nusselt number correlations require further clarifications with respect to their impact on the whole engine performance modeling. For the limited heat-exchanger areas presented in this paper a -+15 % variation in heat-transfer coefficient will result in a -+3% variation in fuel temperature (-+5 K), which will result in a cruise SFC variation of about -+0.08 %, whereas cruise NOx will vary by about -+1%.

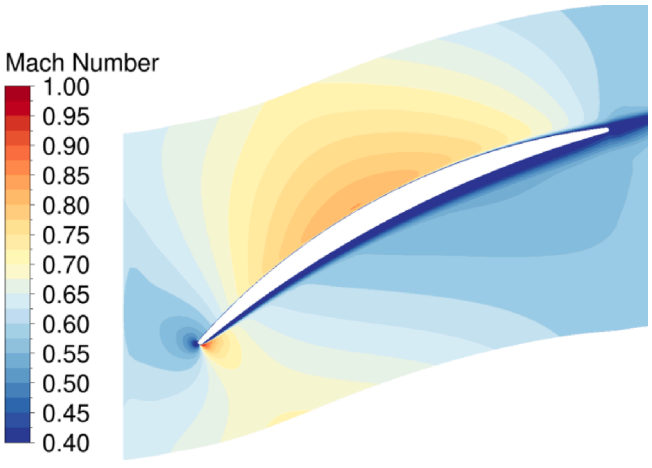

Fig. 19. Mach number contour for stator S1 at midspan. The separation near the leading edge of the pressure side is clearly visible.

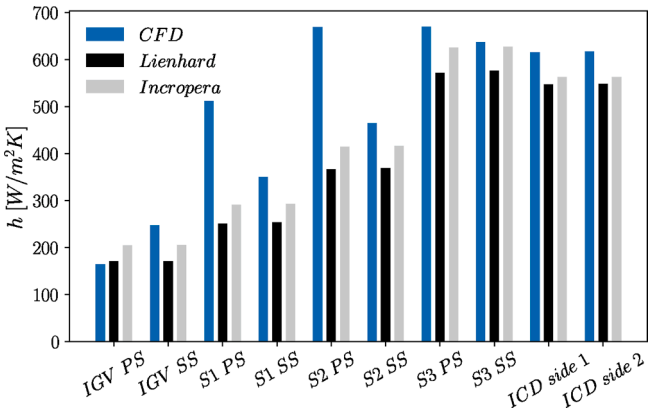

Fig. 20. Average heat transfer coefficient for the VINK stator blades. The blue bar denotes area-averaged values from CFD, the black bar (Lienhard) the numerically calculated average of Eq. (14) at midspan, while the grey bar (Incropera) corresponds to Eq. (9), also evaluated at midspan. (For interpretation of the references to colour in this figure legend, the reader is referred to the web version of this article.)

Table 3
Total pressure loss coefficients $\xi = (p_{0.in} - p_{0.out})/p_{dyn,in}$ for stators in the fully turbulent and transitional cases.

	Turbulent	Transitional	Difference turb. vs trans.
IGV	0.0262	0.0203	+29 %
S1	0.0349	0.0308	+13 %
S2	0.0282	0.0222	+27 %
S3	0.0422	0.0368	+15 %
ICD	0.0543	0.0567	−4%

In Fig. 22 the corner points defining the low-pressure compressor-intercooler geometry are shown together with relevant geometrical and performance data in Table 6. The geometrical and performance data is similar to the VINK geometry previously simulated in section 3.2. A maximum temperature drop of 8.7 K at take-off is observed on the air-side, whereas in the hydrogen side the maximum registered temperature increase is on the order of 56 K for stator 1 at take-off conditions. The larger variation in hydrogen side heat-transfer coefficient is due to the assumption of even hydrogen split across the vanes, which vary in size. At the same time, the cross-sectional area of the individual channels is assumed to be the same, which means that the hydrogen velocity inside the tubes will vary for the various vanes, affecting the Reynolds number.

4. Conclusions

This paper has investigated the heat transfer potential of the stator surfaces in a modern LPC which incorporates cooling channels underneath the stator vane surfaces, where hydrogen is allowed to flow and

Table 4
2050 performance data assumptions.

Fan efficiency (outer fan, isentropic)	94.0 %
Booster efficiency (polytropic)	92.0 %
Cooling ratio (all points)	0.10
HPC efficiency (polytropic)	92.0 %
HPT Efficiency (isentropic)	91.0 %
LPT efficiency (isentropic)	94.0 %
T4 [K] (ISA, take-off)	1825

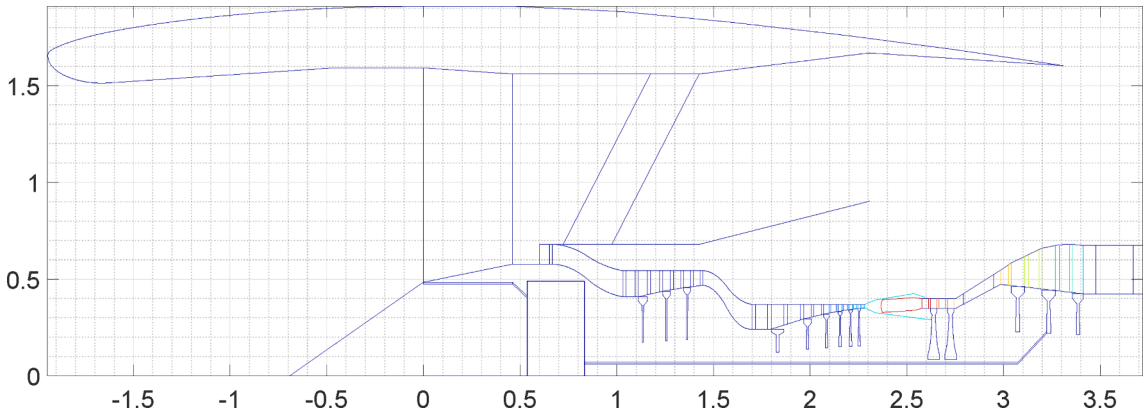

Fig. 21. Schematic engine layout for Y2050 baseline concept.

Table 5
Performance data for the baseline and IPC intercooled engine.

	Baseline (no-intercooling)			Intercooled LPC		
	MTO	MCL	Mid-Cruise	MTO	MCL	Mid-Cruise
Mach number	0	0.84	0.85	0	0.84	0.85
Net thrust [lbf]	84,000	18,100	14,200	84,000	18,100	14,200
T3 (after mixing) [K]	864	803	764	844	789	750
P3 [bar]	42.8	19.5	16.3	42.8	19.5	16.3
T4 [K]	1825	1722	1622	1825	1722	1622
BPR	15.6	15.1	16.6	16	15.4	16.9
FPR	1.5	1.6	1.5	1.5	1.6	1.5
OPR	42	52	43	42	52	43
$\dot{m}_{core}$ [kg/s]	83.9	39.6	34.3	82.1	39.1	33.7
$\dot{m}_{fuel}$ [kg/s]	0.90	0.40	0.31	0.89	0.39	0.31
T_{fuel}(combustor inlet) [K]	100	100	100	151	146	146
SFC [mg/Ns]	2.4	4.92	4.92	2.38	4.88	4.88
EINOx [g/kg fuel]	24.1	11.8	7.84	22.6	11.3	7.56
Fan diameter [m]	3.2			3.2		
Engine weight, inc. nacelle [kg]	9518			9504		

cool the engine core air. The heat transfer potential has been assessed by means of CFD simulations and detailed aerothermal analyses.

Validation of the employed CFD methodology was carried out by comparing numerical simulations with experimental results from the Chalmers low-speed compressor test facility. The experimental and numerical data showed good agreement in terms of span-wise total and dynamic pressure profiles, blade loading, and ICD outlet total pressure, hence affirming the choice of numerical approach.

The cooled VINK compressor featured cooling channels underneath the stator vane surfaces and managed to achieve a core air temperature drop of approximately 9.5 K without incurring additional pressure losses in the core air stream. The total thermal resistance of this cooling approach was seen to be dominated by the air side heat transfer coefficient and was relatively insensitive to the thermal conductivity of the solid material in the vane. Consequently, this was also indicative of a need for more heat transfer surface area on the air side of the stator vanes. The obtained heat transfer levels were for a compressor design which has had no heat transfer considerations in its design. This means that more heat transfer is obtainable if the compressor design is adjusted for more stator surface, i.e., through higher solidity stator blades, or by including cooling channels in the hub and shroud surfaces.

Heat transfer for both fully turbulent and transitional flows was simulated using CFD and compared to flat-plate correlations from literature. While good agreement was found for both types of flows, the heat transfer correlation for the transitional case yields decent accuracy as long as the flow remains attached, and that transition is dominated by the bypass mode. These results were also used to fine-tune the flat plate correlations for use in the system level performance models.

Regarding the system level analysis, the results show a limited impact at engine performance level. More specifically the usage of the static compressor vanes for the purpose of intercooling on large engine results in SFC improvements of 0.7 %-0.9 % in cruise. At the same time, the temperatures drop in the core temperature at the LPC outlet results in a temperature drop at the HPC exit, after mixing with the fuel, allowing for a 2.6 % – 4.6 % reduction in cruise NOx. The results clearly show that, although it is possible to achieve high heat transfer rates per unit area in compressor vanes, the impact on cycle performance is

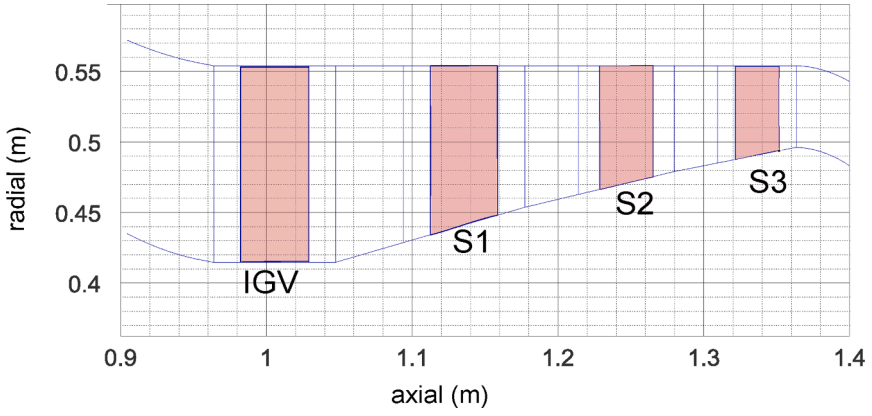

Fig. 22. Corner points defining the low-pressure compressor used for the purpose of intercooling.

Table 6
Design and performance data of the proposed low-pressure compressor-intercooler geometry.

IGV			MTO	MCL	Mid-cruise
HTR	0.75	h_{air} [W/m^2 K]	707	332	281
Number vanes	76	h_{H2} [W/m^2 K]	8420	4259	3446
Aspect ratio	3	Q [kW]	167	65	53
Wetted area [m^2]	1.34	$\Delta T_{0,air}$[K]	−2	−1.7	−1.6
M (design at TOC)	0.5	$\Delta T_{0,H2}$ [K]	47.5	42.3	43.6
Stator 1			MTO	MCL	Mid-cruise
HTR	0.78	h_{air} [W/m^2 K]	819	373	313
Number vanes	88	h_{H2} [W/m^2 K]	7667	3815	3052
Aspect ratio	2.6	Q [kW]	200	78	62
Wetted area [m^2]	1.28	$\Delta T_{0,air}$ [K]	−2.4	−2.0	−1.9
M (design at TOC)	0.5	$\Delta T_{0,H2}$[K]	56.3	49.8	50.7
Stator 2			MTO	MCL	Mid-cruise
HTR	0.84	h_{air} [W/m^2 K]	1044	470	391
Number vanes	93	h_{H2} [W/m^2 K]	8093	4065	3266
Aspect ratio	2.4	Q [kW]	193	76	60
Wetted area [m^2]	0.88	$\Delta T_{0,air}$[K]	−2.3	−2	−1.8
M (design at TOC)	0.5	$\Delta T_{0,H2}$[K]	54.4	48.9	49
Stator 3			MTO	MCL	Mid-cruise
HTR	0.88	h_{air} [W/m^2 K]	1412	627	520
Number vanes	98	h_{H2} [W/m^2 K]	9779	5027	4091
Aspect ratio	2.2	Q [kW]	168	68	53
Wetted area [m^2]	0.51	$\Delta T_{0,air}$[K]	−2	−1.8	−1.6
M (design at TOC)	0.5	$\Delta T_{0,H2}$[K]	47.6	44.0	43.5

constrained due to the limited available wetted area in the low-pressure compressor. One option would be to trigger transition at the leading edge, allowing for an increase in heat-transfer rate of about 20 % as shown in section 3.2.3, at a cost of increasing the pressure loss by 15–30 % for each stator. Another alternative is to increase blade solidity which will also result in increased pressure loss and decreased compressor efficiency. For a constant solidity an increase in the aspect ratio will also result in increased heat-transfer.

The exceptional cooling capacity of hydrogen and possible SFC savings could potentially be realized by incorporating compact heat exchangers in strategic locations in the engine core, thereby increasing the amount of wetted area. This also requires careful integration of heat exchangers and connecting ducts to avoid excessive pressure losses, weight, and volume.

Declaration of Competing Interest

The authors declare the following financial interests/personal relationships which may be considered as potential competing interests: Alexandre Capitao Patrao reports financial support and equipment, drugs, or supplies were provided by Chalmers University of Technology.

Data availability

Data will be made available on request.

Acknowledgements

The work was financed and supported by Chalmers' Areas of Advance Transport project "PATH - Pathways for a sustainable introduction of hydrogen into the aviation sector". Test data from the low-pressure compressor facility at Chalmers Fluid and Thermal Science Laboratory was financed by the E.U. under the "ENABLEH2 – Enabling cryogenic hydrogen-based CO2 free air transport" Project co-funded by the European Commission within the Horizon 2020 Programme (2014-2020) under Grant Agreement no. 769241. The authors also acknowledge the support provided by the department of Mechanics and Maritime Sciences at Chalmers University of Technology. The simulations were enabled by resources provided by the National Academic Infrastructure for Supercomputing in Sweden (NAISS) and the Swedish National Infrastructure for Computing (SNIC) at C3SE partially funded by the Swedish Research Council through grant agreements no. 2022-06725 and no. 2018-05973.

References

[1] European Commision, Communication From The Commission To The European Parliament, The European Council, The Council, The European Economic And Social Committee And The Committee Of The Regions-The European Green Deal., (2019) 1. https://eur-lex.europa.eu/legal-content/EN/TXT/?uri=COM:2019:640:FIN.
[2] E.J. Adler, J.R.R.A. Martins, Hydrogen-Powered Aircraft: Fundamental Concepts, Key Technologies, and Environmental Impacts, Fuel 32 (2022) 7.
[3] G.D. Brewer, Hydrogen aircraft technology, 2017. 10.1201/9780203751480.
[4] D. Jian, Z. Qiuru, Key technologies for thermodynamic cycle of precooled engines: A review, Acta Astronaut. 177 (2020) 299–312, https://doi.org/10.1016/j.actaastro.2020.07.039.
[5] M. Coutinho, D. Bento, A. Souza, R. Cruz, F. Afonso, F. Lau, A. Suleman, F. R. Barbosa, R. Gandolfi, W. Affonso, F.I.K. Odaguil, M.F. Westin, R.J.N. dos Reis, C. R.I. da Silva, A review on the recent developments in thermal management systems for hybrid-electric aircraft, Appl. Therm. Eng. 227 (2023), 120427, https://doi.org/10.1016/j.applthermaleng.2023.120427.
[6] H. Abedi, C. Xisto, I. Jonsson, T. Grönstedt, A. Rolt, Preliminary Analysis of Compression System Integrated Heat Management Concepts Using LH2-Based Parametric Gas Turbine Model, Aerospace 9 (2022), https://doi.org/10.3390/aerospace9040216.
[7] J.J. Murray, A. Guha, A. Bond, Overview of the development of heat exchangers for use in air-breathing propulsion pre-coolers, Acta Astronaut. 41 (1997) 723–729, https://doi.org/10.1016/S0094-5765(97)00199-9.
[8] P. Dong, H. Tang, M. Chen, Study on multi-cycle coupling mechanism of hypersonic precooled combined cycle engine, Appl. Therm. Eng. 131 (2018) 497–506, https://doi.org/10.1016/j.applthermaleng.2017.12.002.
[9] I. Jonsson, C. Xisto, H. Abedi, T. Grönstedt, M. Lejon, Feasibility study of a radical vane-integrated heat exchanger for turbofan engine applications, in: Proc. ASME Turbo Expo, American Society of Mechanical Engineers, 2020, pp. 1–8, https://doi.org/10.1115/GT2020-15243.
[10] Y. Xu, H. Tang, M. Chen, F. Duan, Optimization and design of heat recovery system for aviation, Appl. Therm. Eng. 165 (2020), 114581, https://doi.org/10.1016/j.applthermaleng.2019.114581.
[11] S. Boggia, A. Jackson, Some Unconventional Aero Gas Turbines Using Hydrogen Fuel, in: Vol. 2 Turbo Expo 2002, Parts A B, ASMEDC, 2002: pp. 683–690. 10.1115/GT2002-30412.
[12] I.P. van Dijk, A.G. Rao, J.P. van Buijtene, Stator Cooling & Hydrogen Based Cycle, in: International Symposium on Air Breathing Engines 2009, Montreal, 2009.
[13] F. Svensson, R. Singh, Effects of Using Hydrogen on Aero Gas Turbine Pollutant Emissions, Performance and Design, in: Vol. 2 Turbo Expo 2004, ASMEDC, 2004, pp. 107–116. 10.1115/GT2004-53349.
[14] H. Canière, A. Willockx, E. Dick, M. De Paepe, Raising cycle efficiency by intercooling in air-cooled gas turbines, Appl. Therm. Eng. 26 (2006) 1780–1787, https://doi.org/10.1016/j.applthermaleng.2006.02.008.
[15] P. Shah, N., C. Tan, S., Effect of Blade Passage Surface Heat Extraction on Axial Compressor Performance, J. Turbomach. 129 (2007) 457–467. 10.1115/1.2372776.
[16] L.-G. Liu, X.-S. Li, X.-D. Ren, C.-W. Gu, Investigation of Cooling Effect on the Aerodynamic Performance in the Intercooled Compressor, J. Propul. Power 34 (2018) 920–932, https://doi.org/10.2514/1.B36676.
[17] Y. Ito, T. Nagasaki, Suggestion of Intercooled and Recuperated Jet Engine Using Already Equipped Components as Heat Exchangers, in: In: 47th AIAA/ASME/SAE/ASEE Jt. Propuls, Conf. & Exhib., American Institute of Aeronautics and Astronautics, Reston, Virigina, 2011, pp. 1–16, https://doi.org/10.2514/6.2011-6102.
[18] I. Jonsson, Experimental aerothermal study of internal jet engine structure, Chalmers University of Technology, 2021. https://research.chalmers.se/en/publication/527645.
[19] I. Jonsson, C. Xisto, M. Lejon, A. Dahl, T. Grönstedt, Design and Pre-Test Evaluation of a Low-Pressure Compressor Test Facility for Cryogenic Hydrogen Fuel Integration, in: Vol. 2A Turbomach. — Axial Flow Fan Compress. Aerodyn., American Society of Mechanical Engineers, 2021. 10.1115/GT2021-58946.
[20] I. Jonsson, G. Debarshee, C. Xisto, T. Grönstedt, Design of Chalmers new Low-Pressure Compressor Test Facility for Low-Speed Testing of Cryo-Engine Applications, in: 14th Eur. Conf. Turbomach. Fluid Dyn. Thermodyn. ETC 2021, European Conference on Turbomachinery Fluid dynamics & Thermodynamics, Gdansk, 2021. 10.29008/etc2021-554.
[21] M. Lejon, T. Grönstedt, N. Glodic, P. Petrie-Repar, M. Genrup, A. Mann, Multidisciplinary Design of a Three Stage High Speed Booster, in: In, Vol. 2B, Turbomach., American Society of Mechanical Engineers, 2017, https://doi.org/10.1115/GT2017-64466.
[22] VINK, (n.d.). https://github.com/nikander/VINK.
[23] F.R. Menter, R.B. Langtry, S.R. Likki, Y.B. Suzen, P.G. Huang, S. Völker, A Correlation-Based Transition Model Using Local Variables—Part I: Model Formulation, J. Turbomach. 128 (2006) 413, https://doi.org/10.1115/1.2184352.
[24] R.B. Langtry, F.R. Menter, S.R. Likki, Y.B. Suzen, P.G. Huang, S. Völker, A Correlation-Based Transition Model Using Local Variables—Part II: Test Cases

and Industrial Applications, J. Turbomach. 128 (2006) 423–434, https://doi.org/10.1115/1.2184353.
[25] R. Langtry, F. Menter, Transition Modeling for General CFD Applications in Aeronautics, in: In: 43rd AIAA Aerosp. Sci. Meet, Exhib., American Institute of Aeronautics and Astronautics, Reston, Virigina, 2005, pp. 15513–15526, https://doi.org/10.2514/6.2005-522.
[26] ANSYS Inc., ANSYS CFX-Solver Theory Guide, 2021r1 ed., 2021.
[27] E.W. Lemmon, I.H. Bell, M. Huber, M. McLinden, NIST Standard Reference Database 23: Reference Fluid Thermodynamic and Transport Properties -, 10, REFPROP, version 2018,.
[28] R. Arnold, D. Suslov, O. Haidn, Convective and Film Cooled Nozzle Extension for a High Pressure Rocket Subscale Combustion Chamber, in: In: 48th AIAA Aerosp. Sci. Meet. Incl. New Horizons Forum Aerosp, Expo., American Institute of Aeronautics and Astronautics, 2010, https://doi.org/10.2514/6.2010-1150.
[29] M. Pizzarelli, F. Nasuti, M. Onofri, CFD analysis of transcritical methane in rocket engine cooling channels, J. Supercrit. Fluids 62 (2012) 79–87, https://doi.org/10.1016/j.supflu.2011.10.014.
[30] V. Gnielinski, New equations for heat and mass transfer in turbulent pipe and channel flow, Int. Chem. Eng. 16 (1976) 359–368. https://api.semanticscholar.org/CorpusID:136639967.
[31] B.S. Petukhov, J.P. Hartnett, T.F. Irvine, Adv. Heat Tran. 6 (1970).
[32] T. Grönstedt, Development of methods for analysis and optimization of complex jet engine systems, Chalmers University of Technology, 2000. https://publications.lib.chalmers.se/records/fulltext/799.pdf.
[33] G. Sanford, B.J. McBride, Computer Program for Calculation of Complex Chemical Equilibrium Compositions and Applications. NASA Reference Publication, 1311, Cleveland, Ohio, 1994.
[34] A. Rolt, V. Sethi, F. Jacob, J. Sebastiampillai, C. Xisto, T. Grönstedt, L. Raffaelli, Scale effects on conventional and intercooled turbofan engine performance, Aeronaut. J. 121 (2017) 1162–1185, https://doi.org/10.1017/aer.2017.38.
[35] A. Capitao Patrao, C. Xisto, I. Jonsson, A. Lundbladh, D2.4 – Final report on heat management system, 2023. https://ec.europa.eu/research/participants/documents/downloadPublic?documentIds=080166e5f6b47829&appId=PPGMS.
[36] F.P. Incropera, D.P. DeWitt, T.L. Bergman, A.S. Lavine, Fundamentals of Heat and Mass Transfer, 6th ed., Wiley, New York, 2007.
[37] J.H. Lienhard, Heat Transfer in Flat-Plate Boundary Layers: A Correlation for Laminar, Transitional, and Turbulent Flow, J. Heat Transfer 142 (2020), https://doi.org/10.1115/1.4046795.
[38] R.E. Mayle, The 1991 IGTI Scholar Lecture: The Role of Laminar-Turbulent Transition in Gas Turbine Engines, J. Turbomach. 113 (1991) 509–536. 10.1115/1.2929110.
[39] W.M. Kays, A.L. London, Compact Heat Exchangers, 2nd ed., McGraw-Hill, 1984.
[40] V. Chernoray, J. Hjärne, Improving the Accuracy of Multihole Probe Measurements in Velocity Gradients, in: Vol. 2 Control. Diagnostics Instrumentation; Cycle Innov. Electr. Power, ASMEDC, 2008: pp. 125–134. 10.1115/GT2008-50492.
[41] C.J. Clark, S.D. Grimshaw, A Pneumatic Probe for Measuring Spatial Derivatives of Stagnation Pressure, in: Vol. 6 Ceram. Control. Diagnostics, Instrumentation; Educ. Manuf. Mater. Metall., American Society of Mechanical Engineers, 2019: pp. 1–12. 10.1115/GT2019-91428.
[42] J. Coull, T. Dickens, H. Ng, J. Serna, Five hole probe errors caused by fluctuating incidence, E3S Web Conf. 345 (2022) 01006, https://doi.org/10.1051/e3sconf/202234501006.
[43] J.D. Denton, Loss Mechanisms in Turbomachines, in: Vol. 2 Combust. Fuels; Oil Gas Appl. Cycle Innov. Heat Transf. Electr. Power; Ind. Cogener. Ceram. Struct. Dyn. Control. Diagnostics Instrumentation; IGTI Sch. Award, American Society of Mechanical Engineers, 1993. 10.1115/93-GT-435.